Absolute quantitation of individual SARS-CoV-2 RNA molecules: a new paradigm for infection dynamics and variant differences

Jeffrey Y Lee[1&], Peter AC Wing[2,3&], Dalia S Gala[1], Aino I Järvelin[1], Josh Titlow[1], Marko Noerenberg[4], Xiaodong Zhuang[2], Natasha Johnson[4], Louise Iselin[1], Mary Kay Thompson[1], Richard M Parton[1], Alan Wainman[5], Daniel Agranoff[6], William James[5], Alfredo Castello[1,4*], Jane A McKeating[2,3*] and Ilan Davis[1*].

*Joint corresponding authors: Ilan.davis@bioch.ox.ac.uk Jane.mckeating@ndm.ox.ac.uk alfredo.castello@glasgow.ac.uk [&]Contributed equally to the work

1. Department of Biochemistry, The University of Oxford, UK.
2. Nuffield Department of Medicine, University of Oxford, Oxford, UK.
3. Chinese Academy of Medical Sciences (CAMS) Oxford Institute (COI), University of Oxford, Oxford, UK.
4. MRC-University of Glasgow Centre for Virus Research, The University of Glasgow, UK.
5. Sir William Dunn School of Pathology, University of Oxford, UK.
6. Brighton and Sussex University Hospitals NHS Trust, UK.

Highlights (96 characters or fewer with spaces)

- Single molecule quantification of SARS-CoV-2 replication uncovers early infection kinetics
- There is substantial heterogeneity between cells in rates of SARS-CoV-2 replication
- Genomic RNA is stable and persistent during the initial stages of infection
- Alpha (B.1.1.7) variant of concern replicates more slowly than the Victoria strain

Summary

Despite an unprecedented global research effort on SARS-CoV-2, early replication events remain poorly understood. Given the clinical importance of emergent viral variants with increased transmission, there is an urgent need to understand the early stages of viral replication and transcription. We used single molecule fluorescence *in situ* hybridisation (smFISH) to quantify positive sense RNA genomes with 95% detection efficiency, while simultaneously visualising negative sense genomes, sub-genomic RNAs and viral proteins. Our absolute quantification of viral RNAs and replication factories revealed that SARS-CoV-2 genomic RNA is long-lived after entry, suggesting that it avoids degradation by cellular nucleases. Moreover, we observed that SARS-CoV-2 replication is highly variable between cells, with only a small cell population displaying high burden of viral RNA. Unexpectedly, the Alpha variant, first identified in the UK, exhibits significantly slower replication kinetics than the

Victoria strain, suggesting a novel mechanism contributing to its higher transmissibility with important clinical implications.

Graphical Abstract

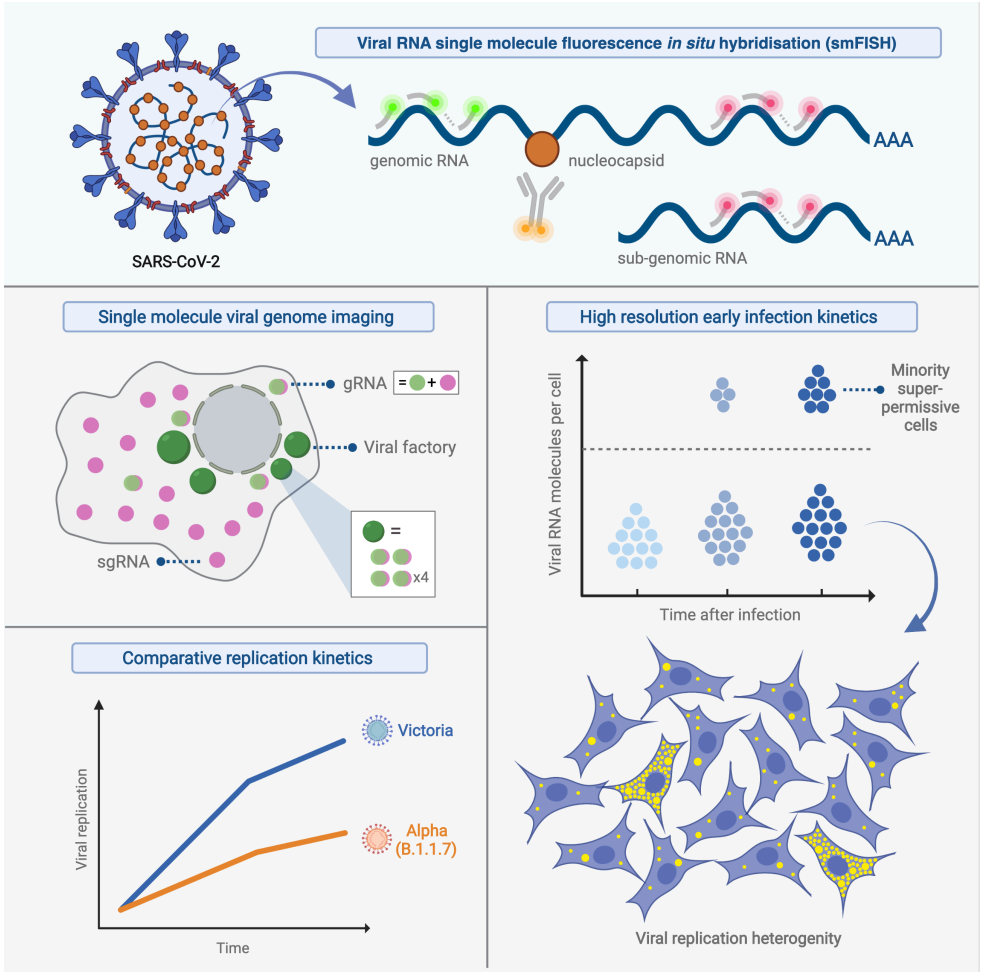

In brief (45 words / 50-word limit)

By detecting nearly all individual SARS-CoV-2 RNA molecules we quantified viral replication and defined cell susceptibility to infection. We discovered that a minority of cells show significantly elevated viral RNA levels and observed slower replication kinetics for the Alpha variant relative to the Victoria strain.

Keywords COVID-19; SARS-CoV-2 virus; Variant of concern; B.1.1.7; Victoria; Alpha; single molecule fluorescence in situ hybridisation (smFISH); mRNA stability; early replication

Introduction

Severe acute respiratory syndrome coronavirus 2 (SARS-CoV-2) is the causative agent of the COVID-19 pandemic. The viral genome consists of a single 30kb positive strand genomic RNA (gRNA) that encodes a plethora of viral proteins (Kim et al., 2020; Zhao et al., 2021). SARS-CoV-2 primarily targets the respiratory tract and infection is mediated by Spike protein binding to human angiotensin-converting enzyme (ACE2) where the transmembrane protease serine 2 (TMPRSS2) triggers fusion of the viral and cell membranes (Hoffmann et al., 2020; Wan et al., 2020). Following virus entry and capsid trafficking to the endoplasmic reticulum, the first step in the replicative life cycle is the translation of the gRNA to form the replicase complex. This complex synthesizes the negative sense genomic strand, enabling the synthesis of additional positive gRNA copies. In addition, a series of shorter sub-genomic (sg)RNAs are synthesised that encode the matrix, spike, nucleocapsid and envelope structural as well as the non-structural proteins (Kim et al., 2020; Sola et al., 2015). The intracellular localisation of these early events were described using electron microscopy (Laue et al., 2021) and by antibody-based imaging of viral double stranded (ds)RNA (Lean et al., 2020). However, this method of detecting dsRNA lacks sensitivity and specificity at early times post infection, as the low abundance of SARS-CoV-2 dsRNA is indistinguishable from host dsRNAs (Dhir et al., 2018). Our current knowledge on these early steps in the SARS-CoV-2 replicative life cycle are poorly understood despite their essential role in the establishment of productive infection.

Since the initial outbreak in the Wuhan province of China in 2019 several geographically distinct variants of concern (VOC) with altered transmission have arisen (Chen et al., 2020; Lythgoe et al., 2021). Emerging VOC such as the B.1.1.7 strain (recently renamed Alpha), first detected in Kent in the UK, possess a fitness advantage in terms of their ability to transmit compared to the Victoria isolate, an early Wuhan-related strain of SARS-CoV-2 (Caly et al., 2020; Davies et al., 2021; Kidd et al., 2021; Volz et al., 2021). Many of the VOC encode mutations in the Spike protein (Rees-Spear et al., 2021) and, consequently, the effects of these amino acid substitutions on viral entry and immuno-evasion are under intense study (Kissler et al., 2021; Washington et al., 2021). However, some of the mutations map to non-structural proteins, and it is thus plausible that they impact viral replication dynamics. Unfortunately, the replication kinetics of SARS-CoV-2 variants remains poorly understood, as the current techniques for quantifying SARS-CoV-2 genomes and replication rates rely on bulk approaches or have limited sensitivity.

The use of single molecule and single-cell analyses in biology offers unprecedented insights into the behaviour of individual cells and the stochastic nature of gene expression that are often masked by population-based studies (Fraser and Kaern, 2009; Raj and van Oudenaarden, 2009). In virology these approaches have revealed how cells vary in their ability to support viral growth and how stochastic forces can inform our understanding of the infection process (Billman et al., 2017; Boersma et al., 2020; Chou and Lionnet, 2018; Shulla and Randall, 2015; Singer et al., 2021). Fluorescence in situ hybridisation (FISH) was previously used to detect RNAs in hepatitis C virus and Sindbis infected cells with high sensitivity (Garcia-Moreno et al., 2019; Ramanan et al., 2016; Singer et al., 2021). However, this approach has only been applied to SARS-CoV-2 in a limited capacity (Burke et al., 2021; Rensen et al., 2021) with the majority of studies utilising amplification-based signal detection methods to visualise viral RNA (Best Rocha et al., 2020; Carossino et al., 2020; Guerini-Rocco et al., 2020; Jiao et al., 2020; Kusmartseva et al., 2020; Lean et al., 2020; Liu et al., 2020). These experiments used either chromogenic histochemical detection using bright field microscopy, or detection of fluorescent dyes, which both lack the sensitivity to detect individual RNA molecules. Consequently, the kinetics of SARS-CoV-2 RNA replication and transcription during the early phase of infection are not well understood and lack quantitative, spatial and temporal information on the genesis of gRNA and sgRNAs. To address this gap, we developed a single molecule (sm)FISH method based on earlier published protocols (Femino et al., 1998; Raj et al., 2008; Singer et al., 2021; Titlow et al., 2018) to visualise SARS-CoV-2 RNAs with high sensitivity and spatial precision, providing a powerful new approach to track infection and to detect and quantify viral replication factories. Our results uncover a previously unrecognised heterogeneity among cells in supporting SARS-CoV-2 replication and a surprisingly slower replication rate of the Alpha B.1.1.7 variant when compared to the Victoria strain.

Results

SARS-CoV-2 genomic RNA at single molecule resolution.

To explore the spatial and temporal aspects of SARS-CoV-2 replication at single molecule and cell levels we carried out smFISH experiments with fluorescently labelled probes directed against the 30kb viral genomic RNA. 48 short antisense DNA oligonucleotide probes were designed to target the viral ORF1a and labelled with a single fluorescent dye to detect the positive sense gRNA (+gRNA), as described previously (Gaspar et al., 2017) (Figure 1A). The probe set detected single molecules of gRNA within SARS-CoV-2 infected Vero E6 cells, visible as well-resolved diffraction-limited single spots with a consistent fluorescence intensity and shape (Figure 1B). Treatment of the infected cells with RNase or the viral polymerase

inhibitor remdesivir (RDV) ablated the probe signal, confirming specificity (Figure S1A). To assess the efficiency and specificity of detection of the ORF1a probe set, we divided the probes into two groups of 24 alternating oligonucleotides (“ODD” and “EVEN”) that were labelled with different fluorochromes. Interlacing the probes minimised chromatic aberration between spots detected by the two colours (Figure 1C). Analysis of the SARS-CoV-2 gRNA with these probes showed a mean distance of <250nm between the two fluorescent spots, indicating near-perfect colour registration and a lack of chromatic aberration. 95% of the diffraction-limited spots within infected cells were dual labelled, demonstrating efficient detection of single SARS-CoV-2 gRNA molecules (Figure 1C).

To assess the specificity of the ORF1a probes we aligned them against other coronaviruses and the human transcriptome. Many of the oligonucleotides showed mismatches with SARS-CoV-1, MERS and other coronaviruses along with human RNAs (Figure 1D). We also evaluated their ability to bind HCoV-229E RNA within infected Huh-7 cells. Although the J2 antibody, specific for double stranded (ds)RNA, detected dsRNA foci in the HCoV-229E infected cells, no signal was seen with the SARS-CoV-2 ORF1a probe set (Figure S1B). Taken together, these results highlight the efficiency and specificity of the ORF1a probe set for detecting single molecules of SARS-CoV-2 gRNA.

Having established smFISH for the detection of SARS-CoV-2 gRNA we used this technique to assess both the quantity and distribution of gRNA during infection. Cells were inoculated with virus (MOI 1) for 2h and non-internalised virus removed by trypsin digestion, allowing us to synchronise the infection. At 2 hours post infection (hpi), the majority of fluorescent spots correspond to single gRNAs along with a small number of foci harbouring several gRNA copies (Figure 1E), consistent with early RNA replication events. By 8 hpi, we noted an expansion in the number of bright multi-gRNA foci and at 24 hpi there was a further increase in the number of multi-RNA foci that localised to the perinuclear region, consistent with the reported association of viral replication factories with membranous structures derived from the endoplasmic reticulum (V'Kovski et al., 2021) (Figure 1E). Interestingly, individual gRNA molecules were still detected, especially, at the periphery of cells that may correspond to viral particles (Kamel et al., 2021). To assess whether virion-associated RNA is accessible to the probes, we incubated immobilized SARS-CoV-2 particles with the ORF1a probes. We observed a large number of spots in the immobilised virus preparation that was compatible with single RNA molecules (Figure S1C), suggesting the detection of RNA in viral particles. In

summary, detection of SARS-CoV-2 +gRNA by smFISH identifies changes in viral RNA abundance and cellular distribution during early replication.

Quantification of SARS-CoV-2 genomic and sub-genomic RNAs.

SARS-CoV-2 produces both gRNA and subgenomic (sg)RNAs which are both critical to its replicative life cycle. However, quantitation of sgRNAs is challenging due to their sequence overlap with the 3' end of the gRNA. To estimate the abundance of sgRNAs we designed two additional probe sets labelled with different fluorochromes; an ORF-N set that hybridises to all canonical positive sense viral RNAs, and an ORF-S set that detects only S-sgRNA and gRNA (Figure 2A) (Kim et al., 2020). Therefore, spots showing fluorescence only for ORF-N or ORF-S probe sets will represent sgRNAs, whereas spots positive for both ORF-N or ORF-S and ORF1a will correspond to gRNA molecules. We applied this approach to visualise SARS-CoV-2 RNAs in infected Vero E6 cells (6 hpi) and observed a high abundance of sgRNAs compared with gRNAs (Figure 2B), in agreement with RNA sequencing studies (Alexandersen et al., 2020; Kim et al., 2020). Further analysis revealed that the ORF-N and ORF-S single labelled spots were more uniformly distributed throughout the cytoplasm than dual labelled gRNA, consistent with their predominant role as mRNAs to direct protein synthesis (Figure 2B). Association of gRNA with nucleocapsid (N) is essential for the assembly of coronavirus particles (Carlson et al., 2020; Dinesh et al., 2020; Iserman et al., 2020). To monitor this process in SARS-CoV-2, we combined smFISH with the ORF1a and ORF-N probe sets and immunofluorescence with an antibody against N. Our findings show that N protein primarily co-localises with gRNA, while displaying a limited overlap with sgRNAs (Figure 2C). These data show the specificity of our probes to discriminate between the viral gRNA and sgRNAs.

Negative sense gRNA and sgRNAs are the templates for the synthesis of positive sense RNAs and are expected to localise to viral replication factories. However, their detection by RT-qPCR or sequencing is hampered by cDNA library protocols that employ oligo(dT) selection and by primer binding to dsRNA structures (Ramanan et al., 2016; Sethna et al., 1991). To detect negative sense viral RNAs we denatured dsRNA through either formamide, DMSO or sodium hydroxide treatment (Singer et al., 2021; Wilcox et al., 2019). The combination of DMSO with heat treatment resulted in a loss of anti-dsRNA J2 signal, while maintaining cell integrity, suggesting a disruption of dsRNA hybrids (Figure S2A). We designed an smFISH probe set specific for the ORF1b antisense sequence that targets the negative sense gRNA (-gRNA) and resulted in intense diffraction-limited spots in DMSO and heat-treated cells (Figure 2D). The -gRNA spots were detected at a significantly lower level than their +gRNA counterparts,

with substantial overlap observed between the two strands at multi-RNA spots, consistent with these foci representing active sites of viral replication. To determine if these multi-RNA foci contain dsRNA, the permeabilised infected cells were treated with RNaseT1 or RNaseIII, which are nucleases specific for single-stranded RNA (ssRNA) and dsRNA, respectively (Figure S2B). RNaseT1 digestion diminished the +gRNA probe signal, while RNaseIII treatment abolished the anti-dsRNA J2 signal. A cocktail of RNaseT1 and RNaseIII ablated both +ORF1a probe binding and anti-dsRNA J2 signals, demonstrating that the ORF1a probe set hybridises to both single and duplex RNA under our experimental conditions (Figure S2B). Furthermore, treating cells with DMSO prior to RNaseT1 fully ablated the smFISH signal (Figure S2C), demonstrating that denaturation makes dsRNA accessible for RNaseT1 degradation. In summary, our data showing that probe binding to negative strand gRNA requires chemical denaturation, suggesting that this replication intermediate localise within dsRNA structures.

Anti-dsRNA antibodies underestimate SARS-CoV-2 replication.

The establishment of replication factories is a critical phase of the virus life cycle. Previous reports have Identified these viral cellular factories using the J2 dsRNA antibody (Burgess and Mohr, 2015; Cortese et al., 2020; Targett-Adams et al., 2008; Weber et al., 2006). However, this approach depends on high levels of viral dsRNA as cells naturally express endogenous low levels of dsRNA (Dhir et al., 2018; Kimura et al., 2018) (Figure 2E). To evaluate the ability of J2 antibody to quantify SARS-CoV-2 replication sites, we co-stained infected cells at 2 and 6 hpi with both J2 and ORF1a smFISH probes. No viral-specific J2 signal was detected at 2 hpi and only 10% of infected cells stained positive at 6 hpi, in agreement with previous observations (Cortese et al., 2020; Eymieux et al., 2021) (Figure 2E). In contrast, more than 85% of the cells showed diffraction-limited smFISH signals at both time points (Figure 2F). Furthermore, the average J2 signal detected in the SARS-CoV-2 infected cells at both time points was comparable to uninfected cells (Figure 2F). These data clearly show the J2 antibody, although broadly used, underestimates the frequency of SARS-CoV-2 infection. In contrast, smFISH detected gRNA as early as 2 hpi, with a significant increase in copy number by 6 hpi, highlighting its utility to detect and quantify viral replication factories.

SARS-CoV-2 replication at single molecule resolution.

The efficiency and sensitivity of the smFISH approach to detect single molecules of SARS-CoV-2 RNA allows us to investigate the dynamics of viral replication in Vero E6 cells during the first 10h of infection (Figure 3A). At 2 hpi the +ORF1a probe set detected predominantly

single molecules of +gRNA with a median value of ~30 molecules per cell (Figure 3B-C). Of note, gRNA copies/cell at 2hpi were unaffected by RDV treatment, suggesting that these RNAs derive from incoming viral particles (Figure 3C). In contrast, the increase in gRNA copies/cell at 4 and 6 hpi was inhibited by RDV, reflecting active viral replication. The infected cell population showed varying gRNA levels that we classified into three groups; (i) 'partially resistant' cells with $<10^2$ gRNA copies that showed no increase between 2 and 8 hpi (60% of the population); (ii) 'permissive' cells with $\sim10^2$-10^5 copies/cell showing a modest increase in gRNA burden over the time of the experiment (~30%) and (iii) 'super-permissive' cells with $>10^5$ copies/cell showing a dramatic increase in gRNA copies (~10%). RDV treatment delayed the appearance of super-permissive cells until late times post infection (10-24 hpi) (Figure 3C-E). RDV inhibition of viral replication was partial despite using a concentration that exceeded the IC90 as defined using bulk RT-qPCR method (Figure S3A). Analysing the total cellular gRNA content showed the dominant source of vRNA to be the 'super-permissive' cells (Figure 3D), suggesting that bulk RNA analyses such as RT-qPCR are biased by these 'super-permissive' cells. In the presence of RDV the average gRNA copies/cell were stable over time, suggesting that incoming gRNA is long lived.

Our high-throughput FISH intensity analysis showed that this cellular heterogeneity persists beyond the primary rounds of infection. At 24 hpi 40% of the cells in the population did not reach the super-permissive state but formed a distinct population with approximately 10-fold less gRNA (Figure 3C and E). Of note, the high level of gRNA in super-permissive cells ($\sim10^7$ counts/cell) was comparable over the time course of the experiment, suggesting an upper limit of vRNA copies in Vero E6 cells (Figure 3C). A similar distribution of gRNA was observed between 24-48 hpi, although the levels of gRNA started to decline which may reflect cytolytic effects and virus egress (Figure S3B-D). Treating infected cells at 24 hpi with RDV had a modest effect on gRNA levels (Figure S3D) and reduced the cytolytic effects (Figure S3E), consistent with the long-lived nature of +gRNA within infected cells.

Simultaneous analysis of +ORF1a and +ORF-N revealed similar expression kinetics for sgRNA, with 11 copies/cell of sgRNA detected in 63% of infected cells at 2 hpi (Figure 3C and 3F). Since +sgRNA requires -sgRNA template for its production, our results imply that multiple rounds of transcription occur rapidly following virus internalisation that are RDV insensitive. By 6 hpi, most cells contain sgRNA (Figure 3F), with the super-permissive cells supporting high levels of sgRNA transcription.

We examined the vRNA replication dynamics and found the ratio of sgRNA/gRNA ranged from 0.5-8 over time (Figure 3G), consistent with a recent report in diagnostic samples (Alexandersen et al., 2020). Notably, the sgRNA/gRNA ratio increased between 2 and 10 hpi, followed by a decline at 24 hpi, indicating a shift in preference to produce gRNA over sgRNA in later stages of infection. A similar trend was observed in RDV-treated cells, with a reduced sgRNA/gRNA peak at 8-10 hpi. We estimated the sgRNA/gRNA ratio for individual cells and found that sgRNA synthesis is favoured in the 'partially resistant' and 'permissive' cells, whereas the 'super-permissive' cells had a reduced ratio of sgRNA/gRNA (Figure 3H). In summary, these results indicate that gRNA synthesis is favoured in the late phase of infection, that may reflect the requirement of gRNA to assemble new viral particles.

Positive-sense RNA viruses, including coronaviruses, utilise host membranes to generate viral factories, which are sites of active replication and/or virus assembly (Wolff et al., 2020). Our current knowledge on the genesis and dynamics of these factories in SARS-CoV-2 infection is limited. We exploited the spatial resolution of smFISH to study these structures, which we define as spatially extended foci containing at least 4 gRNA molecules. We observed 1-2 factories per cell at 2 hpi, which increased to ~30 factories/cell by 10 hpi (Figure 3I). In addition, the average number of gRNA molecules within these factories, although variable, increased over time (Figure 3J). RDV treatment reduced both the number of viral factories per cell and their RNA content. Together these data show the capability of smFISH to localise and quantify active sites of SARS-CoV-2 replication and to measure changes in gRNA and sgRNA at a single cell level over the course of the infection.

Super-permissive cells are randomly distributed.

Our earlier kinetic analysis of infected Vero E6 cells identified a minor population of 'super-permissive' cells containing high gRNA copies at 8 hpi. A random selection of ~300 cells allowed us to further characterise the infected cell population (Figure 4A-B). To extend these observations we examined the vRNAs in two human lung epithelial cell lines, A549-ACE2 and Calu-3, that are widely used to study SARS-CoV-2 infection (Chu et al., 2020; Hoffmann et al., 2020). In agreement with our earlier observations with Vero E6, 3-5% of A549-ACE2 and Calu-3 cells showed a 'super-permissive' phenotype (Figure 4C-D). An important question is how these 'super-permissive' cells are distributed in the population, as the pattern could highlight potential drivers for susceptibility (Healy et al., 2020). Infection can induce innate signalling that can lead to the expression and secretion of soluble factors such as interferons that induce an anti-viral state in the local cellular environment (Belkowski and Sen, 1987;

Schoggins and Rice, 2011). Regulation can be widespread through paracrine signalling or affect only proximal cells. We considered three scenarios where 'super-permissive' cells are: randomly distributed, evenly separated spatially in the population or clustered together. We compared the average nearest neighbour distance between 'super-permissive' cells and simulated points that were distributed either randomly, evenly or in clusters (Figure S4A-C). In summary, our results show conclusively that the 'super-permissive' infected Vero E6, A549-ACE2 and Calu-3 cells were randomly distributed (Figure 4E-F and S4D-E). We interpret these data as being consistent with an intrinsic property of the cell that defines susceptibility to virus infection. The data also argue against cell-to-cell signalling mechanisms that would either lead to clustering (if increasing susceptibility) or to an even distribution (if inhibiting) of infected cells.

Differential replication kinetics of the Alpha B.1.1.7 and Victoria strains.

The recent emergence of SARS-CoV-2 VOC, which display differential transmission, pathogenesis and infectivity, have changed the course of the COVID-19 pandemic. Recent studies have focused on mutations in the Spike protein and whether these alter particle uptake into cells and resistance to vaccine or naturally acquired antibodies (Collier et al., 2021; Dicken et al., 2021; Planas et al., 2021). The B.1.1.7 VOC, now designated the Alpha variant, is associated with higher transmission (Davies et al., 2021; Galloway et al., 2021; Volz et al., 2021) and has 17 coding changes mapping to both non-structural (ORF1a/b, ORF3a, ORF8) and structural (Spike and N) proteins. Mutations within the non-structural genes could affect virus replication, independent of Spike mediated entry (Figure 5A). We used smFISH to compare the replication kinetics of the B.1.1.7 and Victoria strains. The number of gRNA molecules at 2 hpi was similar for both viruses, reflecting similar cell uptake of viral particles (Figure 5B-D). However, the quantities of intracellular gRNA and sgRNA were lower in B.1.1.7 infected cells compared to Victoria at 6 and 8 hpi (Figure 5B). We also noted that while the amount of gRNA per cell was reduced in the B.1.1.7 variant, there were an equal number of ORF1a and ORF-N positive cells (Figure 5E), suggesting that the reduced B.1.1.7 RNA burden is due to a differential replication efficiency rather than infection rate. The B.1.1.7 variant also showed a reduced number of replication factories per cell, with each focus containing on average a lower number of gRNA molecules compared to the Victoria strain (Figure 5F-G). The frequency of super-permissive cells was lower for B.1.1.7 at 6 and 8 hpi (Figure 5H and S5A-B) and their distribution was random (Figure S5C). RDV treatment ablated the differences between the viral strains, demonstrating that the observed phenotype is replication-dependent (Figure 5B, E, G).

To confirm that our results with the B.1.1.7 variant are not limited to Vero E6 cells, we assessed replication fitness of both variants in A549-ACE2 cells that were recently reported to be immunocompetent (Li et al., 2021). Both Victoria and B.1.1.7 infection resulted in comparable numbers of infected cells and similar gRNA copies/cell at 2 hpi, demonstrating similar cell entry properties (Figure S6A). However, infection with the B.1.1.7 variant led to a reduced gRNA and sgRNA cellular burden at 8 and 24 hpi (Figure 6A-B and S6B-C). Moreover, fewer 'super-permissive' cells were detected at these time points (Figure 6C). We interpret these results as showing that the Alpha B.1.1.7 variant has reduced replication kinetics in cells with an active antiviral response.

We confirmed these observations by sequencing ribo-depleted total RNA libraries of B.1.1.7 or Victoria strain infected A549-ACE2 cells at 2, 8 and 24 hpi (Figure 6A & S6D). As expected, the number of reads mapping to SARS-CoV-2 genome increased over time, reflecting active replication and transcription (Figure 6D). Reads mapping to the 3' end of the genome increased relative to the 5' end, reflecting the synthesis of sgRNAs (Figure 6D). In agreement with smFISH, we detected similar levels of vRNA at 2 hpi within B.1.1.7 or Victoria infected cells, consistent with similar internalization rates in A549-ACE2 cells (Figure 6E). However, the abundance of vRNAs in the B.1.1.7 infected cells at 8 and 24 hpi was lower than the Victoria strain (Figure 6D-E). Furthermore, the level of B.1.1.7 RNA changed very little between 2 and 8 hpi, and then increased dramatically at 24 hpi. This profile contrasts with Victoria infected cells, that showed a continuous increase in vRNA over time. Together, these results show the Alpha B.1.1.7 variant has delayed replication kinetics.

Transcriptomic changes in B.1.1.7 and Victoria infected cells.

To explore the differences in RNA replication between B.1.1.7 and Victoria strains we assessed the abundance of the different vRNAs. As our RNA-seq analysis was performed with cDNA produced from ribosome-depleted total RNA, we were able to quantify the negative sense viral RNAs that lack poly(A) tail and will be depleted in oligo(dT)-based approaches. In agreement with our smFISH results (Figure 2G), negative sense viral RNAs represented a small fraction of the total vRNA present in the cell (Figure 6F). Small numbers of negative sense vRNA transcripts were already detectable at 2 hpi, supporting our earlier conclusion that viral replication occurs very early, at least in the ~60% of the cell population identified by smFISH (Figure 3C). The level of negative sense vRNAs increased through the time course for the Victoria strain, but in the case of B.1.1.7 we observed a modest reduction between 8 and 24 hpi (Figure 6F).

To assess whether B.1.1.7 showed a delayed expression of sgRNAs, we quantified the reads mapping to the junctions derived from RNA-dependent RNA polymerase discontinuous replication (Kim et al., 2020; V'Kovski et al., 2021). In agreement with smFISH data, sgRNAs were detected in low quantities at 2 hpi (Figure 6D and G) and we observed a rise and fall in sgRNA/gRNA count ratio in the Victoria samples between 8-24 hpi (Figure 6G), in agreement with our single cell smFISH measurements (Figure 3G). In B.1.1.7 infected samples the sgRNA/gRNA ratio was significantly reduced at 8 hpi, suggesting a delayed expression of sgRNAs. Interestingly, B.1.1.7 maintained the sgRNA/gRNA ratio of ~ 4.5 until 24 hpi (Figure 6G), suggesting an extended window of sgRNA expression. In summary, these transcriptomic data confirm our smFISH analyses and highlight the altered kinetics of sgRNA/gRNA between the Alpha B.1.1.7 and Victoria strains.

Discussion

Our spatial quantitation of SARS-CoV-2 replication dynamics at the single molecule and single cell level provides important new insights into the early rate-limiting steps of infection. Typically, analyses of viral replication are carried out using 'in-bulk' approaches such as RT-qPCR and conventional RNA-seq. While very informative, these approaches lack spatial information and do not allow single cell analyses. Although single cell RNA-seq analyses can overcome some of these issues (Fiege et al., 2021; Ravindra et al., 2021), their low coverage and lack of information regarding the spatial location of cells remains significant limitations. In this study we show smFISH is a sensitive approach that allows the absolute quantification of SARS-CoV-2 RNAs at single molecule resolution. Our experiments show the detection of individual gRNA molecules within the first 2h of infection that most likely reflect incoming viral particles. However, we also observed small numbers of foci comprising several gRNAs that were sensitive to RDV treatment, demonstrating early replication events. We believe these foci represent 'replication factories' as they co-stain with FISH probes specific for negative sense viral RNA and sgRNA.

These data provide the first evidence that SARS-CoV-2 replication occurs within the first 2h of infection and increases over time. This contrasts to our observations with the J2 anti-dsRNA antibody where viral dependent signals were apparent at 6 hpi (Cortese et al., 2020; Eymieux et al., 2021). We noted that co-staining SARS-CoV-2 infected cells with J2 and ORF1a FISH probe set showed a minimal overlap, suggesting that infection may induce changes in cellular dsRNA. The observation that infection can perturb mitochondrial function provides a possible explanation for these observations (Appelberg et al., 2020; Mullen et al., 2021). Importantly,

mitochondrial dsRNAs can engage MDA5-driven antiviral signalling (Dhir et al., 2018), a recently identified key sensor of SARS-CoV-2 (Thorne et al., 2021b; Yin et al., 2021). These findings highlight the utility of smFISH to uncover new aspects of SARS-CoV-2 replication that are worthy of further study.

We found that SARS-CoV-2 gRNA persisted in the presence of RDV, suggesting a long half-life that may reflect the high secondary structure of the RNA genome that could render it refractory to the action of nucleases (Simmonds et al., 2021). smFISH revealed complex dynamics of gRNA and sgRNA expression that resulted in a rapid expansion of sgRNA (peaking at 8hpi), followed by a shift towards the production of gRNA (24 hpi), results that were confirmed by RNAseq. Since a viral particle is composed of thousands of proteins and a single RNA molecule, we interpret the high synthesis of sgRNAs as aiming to fulfill the high demand for structural proteins in the viral particles. Once the structural proteins are available in sufficient quantities, the late shift towards gRNA synthesis may ensure the presence of sufficient gRNA to generate the viral progeny.

Our study shows that cells vary in their susceptibility to SARS-CoV-2 infection, where the majority of cells had low vRNA levels ($<10^2$ copies/cell) but a minor population (4-10% for different tissue cell lines) had much higher vRNA ($>10^5$ copies/cell) at 10 hpi. In contrast the cellular vRNA copies at 2 hpi were comparable, suggesting that this phenotype is not explained by differences in virus entry. These 'super-permissive' cells account for the majority of vRNA within the culture and mask the dominant cell population. Similar results were obtained with Vero E6, Calu-3 and A549-ACE2 suggesting this is a common feature of SARS-CoV-2 infection. As both Calu-3 and A549-ACE2 have intact innate sensing pathways (Cao et al., 2021; Li et al., 2021) unlike Vero cells (Desmyter et al., 1968), this variable susceptibility is unlikely to reflect differential immune activation pathways and is consistent with their random distribution within the culture. Recent scRNA sequencing studies of SARS-CoV-2 infected bronchial cultures identified ciliated cells as the primary target, however only a minority of these cells contained vRNA that may reflect low sequencing depth or variation in susceptibility (Fiege et al., 2021; Ravindra et al., 2021). The human respiratory tract encompasses the nasal passage, large and small airways and bronchioles and our knowledge of the specific cell types and their SARS-CoV-2 RNA burden is limited. Applying smFISH to clinical biopsies and experimentally infected animal samples (Salguero et al., 2021) will allow us to address this important question.

Given the current status of the pandemic, there has been a global effort to understand the biology of emergent VOC with high transmission rates and possible resistance to neutralizing antibodies. The majority of studies have focused on mutations mapping to the Spike glycoprotein as they can alter virus attachment, entry and sensitivity to vaccine induced or naturally acquired neutralizing antibodies. However, many of the mutations map to other viral proteins, including components of the RNA-dependent RNA polymerase complex that could impact RNA replication. Our smFISH analysis revealed that the Alpha B.1.1.7 variant shows slower replication kinetics than the Victoria strain, resulting in lower gRNA and sgRNA copies per cell, fewer viral replication factories and a reduced frequency of 'super-permissive' cells. This delay in B.1.1.7 replication was observed in Vero and A549-ACE2 cells and confirmed by RNA-seq. A recent study reported a higher infectivity of B.1.1.7 in Calu-3 cells compared to the Victoria strain and increased expression of sgRNA encoding the innate antagonist ORF9b (Thorne et al., 2021a). The different replication rates of the viral strains observed in our studies may reflect the cell types used along with the single cell approach we used to quantify vRNA. However, we noted a sustained increase in the ratio of sgRNA/gRNA in B.1.1.7 infected cells, reflecting the variation in sgRNA and gRNA replication rates in these strains.

Emerging VOC, such as B.1.1.7, have been reported to have a fitness advantage in terms of their ability to transmit compared to the Victoria isolate (Caly et al., 2020; Davies et al., 2021; Kidd et al., 2021; Volz et al., 2021). However, the mechanisms underlying increased transmission are not well understood. A recent longitudinal study of nasopharyngeal swabs showed that the Alpha B.1.1.7 variant was associated with longer infection times and yet showed similar peak viral loads to non-B.1.1.7 variants (Kissler et al., 2021). The authors conclude that this extended duration of virus shedding may contribute to increased transmissibility and is consistent with our data showing reduced replication of B.1.1.7 at the single cell level. Replication fitness will be defined by the relationship of the virus with its host cell, aggressive replication is expected to trigger cellular antiviral sensors. In contrast, lower replication may allow the virus to replicate and persist for longer periods before host antiviral sensors are triggered. Such differences, and their impact on host anti-viral responses, are likely to be of key importance for our understanding of the success of viral variants to spread through the population.

Figure legends

Figure 1. Sensitive single-molecule detection of SARS-CoV-2 genomic RNA in infected cells.

(A) Schematic illustration of single-molecule fluorescence in situ hybridisation (smFISH) for detecting SARS-CoV-2 positive strand genomic RNA (+gRNA) within infected cells.

(B) Reference spatial profile of a diffraction-limited +ORF1a smFISH spot. The gradient legend represents relative fluorescence intensity (top). Frequency distribution of smFISH spot intensities, exhibiting a unimodal distribution (bottom).

(C) Assessment of smFISH detection sensitivity by a dual-colour co-detection method. Maximum intensity projected images and corresponding FISH-quant spot detection views of ODD and EVEN probe sets are shown. Scale bar = 5 μm. Density histogram of nearest-neighbour distance from one spectral channel to another (top). Vertical line indicates 300 nm distance. Percentage overlap between spots detected by ODD and EVEN split probes, calculated bidirectionally (bottom).

(D) Heatmap of probe sequence alignment against various Coronaviridae and host transcriptomes. Each column represents individual 20 nt +ORF1a probe sequences. The minimum edit distance represents mismatch scores, where '0' indicates a perfect match. Melting temperatures of each probe at the smFISH hybridisation condition are shown.

(E) Experimental design for visualising SARS-CoV-2 gRNA with smFISH at different time points after infection of Vero E6 cells. Cells were seeded on cover-glass and 24 h later, inoculated with SARS-CoV-2 (Victoria strain at MOI 1) for 2 h. Non-internalised viruses were removed by trypsin digestion and cells fixed at the timepoints shown. Representative 4 μm maximum intensity projection confocal images are shown. Numbers at the bottom left corner indicate dynamic contrast range used to display the image. Magnified view of insets in the upper panels are shown in lower panels. Scale bars = 10 μm or 2 μm.

Figure S1. Specific detection of SARS-CoV-2 RNA using single-molecule fluorescence in situ hybridisation (smFISH).

(A) Specificity of the +ORF1a smFISH probe for SARS-CoV-2 RNA. Vero E6 cells were infected with SARS-CoV-2 (Victoria strain, MOI = 1), fixed at 8 hpi and hybridised with +ORF1a smFISH probe. In the remdesivir (RDV) condition, drug was added to cells at 10 μM during virus inoculation and maintained for the infection period. For RNase digestion, permeabilised cells were treated with a cocktail of RNaseT1 and RNaseIII in the presence of MgCl2 to digest

RNA prior to probe hybridisation. Representative full z-projection (8 µm) confocal images are shown. Scale bar = 10 µm.

(B) Calu-3 (top panels) and Huh-7.5 (lower panels) cells were infected with SARS-CoV-2 (Victoria) and HCoV-229E, respectively, at an MOI of 1, fixed at 24 hpi and hybridised with the SARS-CoV-2-specific +ORF1a probe. In addition, cells were stained with anti-dsRNA (J2) to identify infected cells. Representative single slice confocal images are shown. Scale bar = 10 µm.

(C) Visualisation of SARS-CoV-2 encapsidated RNA with smFISH. Virus was immobilised onto poly-L-lysine-coated coverslips and visualised via the +ORF1a probe. A 1 µm maximum z-projected confocal image is shown. Scale bar = 20 µm or 5 µm.

Figure 2. Dissecting SARS-CoV-2 gene expression using smFISH.

(A) Schematic illustration of transcript specific targeting of SARS-CoV-2 genomic RNA (gRNA) and subgenomic RNA (sgRNA) using smFISH.

(B) Transcript specific visualisation of gRNA and sgRNA in infected (Victoria strain) Vero E6 cells. Cells were infected as in (Figure 1D) and hybridised with probes against +ORF1a & +ORF-N probe at 6 hpi (upper panels) or +ORF1a & +ORF-S probe at 8 hpi (lower panels). Representative 3 µm maximum intensity projected confocal images are shown. Orange circular regions of interest (ROIs) indicate S-sgRNA encoding Spike whereas dual-colour spots (teal-coloured ROIs) represent gRNA. Scale bar = 5, 10 or 20 µm.

(C) Co-detection of viral nucleocapsid (N) with gRNA and sgRNA. Monoclonal anti-N (Ey2B clone) was used for N protein immunofluorescence. Representative 3 µm z-projected confocal images are shown. The inset shows a magnified view of co-localised N and gRNA. Scale bar = 10 µm. Fluorescence profiles of N immunostaining and gRNA smFISH intensity across a 2 µm linear distance are shown in the image inset (lower left). Percentage of co-localised gRNA or sgRNA molecules with N-protein at 6 hpi. Co-localisation was assessed by N fluorescence density within point-spread function ellipsoids of RNA spots over random coordinates. sgRNA were defined as single-coloured spots with +ORF-N probe signal only (n=7) (lower right). Student's t-test. ****, $p<0.0001$.

(D) Detection of both positive and negative genomic RNA by denaturing viral dsRNA with DMSO and heat treatment at 80˚C (upper panels). 3 µm z-projected images of infected Vero E6 cells at 8 hpi are shown. Scale bar = 10 µm. Schematic illustration of +ORF1a and -ORF1b probe targeting regions (lower panel). -ORF1b probe target region does not overlap with +ORF1a target sequences to prevent probe duplex formation.

(E) Comparison of anti-dsRNA (J2) and gRNA smFISH. Full z-projected images of infected Vero E6 cells co-stained with J2 and smFISH are shown. Scale bar = 10 μm.

(F) Percentage of infected cells detected by J2 or smFISH (upper panels). For J2-based quantification, we defined the threshold as 95th percentile fluorescent signal of uninfected cells (Mock) due to the presence of endogenous host-derived signals. Fluorescent positive signals were used for smFISH-based quantification. Data are presented as mean ± S.D. Comparison of quantification results between J2 stain and smFISH (lower panels). Each symbol represents one cell. J2 signal was quantified by fluorescence density over 3D cell volume, which was normalised to the average signal of uninfected control cells (horizontal dotted line). gRNA count represents sum of single-molecule spots and decomposed spots within viral factories. The symbol denoted with '#' is the infected cell shown in Figure 2E. (J2 stain, n=3 independent repeats; smFISH, n=4). One-way ANOVA and Tukey post-hoc test. n.s, not significant; *, $p<0.05$; **, $p<0.01$; ****, $p<0.0001$.

Figure S2. Denaturation of SARS-CoV-2 dsRNA for negative strand detection.

(A) Comparison of double-stranded RNA (dsRNA) denaturation efficiency assessed by the reduction of anti-dsRNA (J2) immunofluorescence. SARS-CoV-2-infected (Victoria strain) Vero E6 cells at 8 hpi were fixed and treated with DMSO, formamide or NaOH (see Materials and Methods) prior to immunostaining. Representative low-magnification single slice confocal images are shown. Formamide treatment with heat resulted in cell detachment from coverslips. Scale bar = 200 μm.

(B) Sensitivity of +ORF1a smFISH and J2 immunofluorescence signal to RNase digestion. Fixed infected cells (24 hpi) were treated with RNaseT1 and/or RNaseIII to digest single-stranded RNA and/or dsRNA, respectively, hybridised with +ORF1a probe and stained with J2. Representative full z-projected confocal images are shown, which are single-molecule contrast matched. Scale bar = 20 μm.

(C) RNaseT1 digestion of denatured dsRNA. Fixed infected cells (8 hpi) were treated as follows: i) DMSO/heat only (left); ii) RNaseT1 then DMSO/heat (centre); or ii) in the reverse order of DMSO/heat and then RNaseT1 (right). Treated cells were hybridised with +ORF1a and -ORF1b probes (see (Figure 2D) for schematics) and stained with J2. RNaseT1 digestion followed by DMSO treatment shows viral dsRNA are resistant to RNaseT1 activity, but DMSO treatment preceding RNaseT1 suggests denatured dsRNA can be targeted by RNaseT1. Full z-projected confocal images are shown. Scale bar = 10 μm.

Figure 3. Profiling SARS-CoV-2 replication kinetics at single-molecule resolution.

(A) Experimental design to profile SARS-CoV-2 replication kinetics using smFISH. Vero E6 cells were seeded on cover-glass and 24 h later, inoculated with SARS-CoV-2 (Victoria strain, MOI = 1) for 2 h. Non-internalised viruses were removed by trypsin digestion and cells fixed at the timepoints shown for hybridisation with +ORF1a and +ORF-N probes. In the remdesivir (RDV) condition, the drug was added to cells at 10 μM during virus inoculation and maintained for the infection period.

(B) Maximum z-projected confocal images of infected cells. Numbers at the bottom left corner indicate dynamic contrast range used to display the image. Scale bar = 10 μm.

(C) Bigfish quantification of +gRNA or +sgRNA RNA counts per cell. sgRNA counts were calculated by subtracting +ORF1a counts from +ORF-N counts per cell. Horizontal line indicates 105 molecules of RNA. 24 hpi samples and the cells harbouring > 10^7 RNA counts were quantified by extrapolating single-molecule intensity. Quantified cells from all replicates are plotted. (2-8 hpi, n≥3; 10 and 24 hpi, n=2). Number of cells analysed (Untreated/RDV): 2 hpi, 373/273; 4 hpi, 798/516; 6 hpi, 370/487; 8 hpi, 1442/1022; 10 hpi, 1175/1102; 24 hpi, 542/249.

(D) Relative contribution of viral gRNA within the infected cell population. The infected cells were classified into three groups based on gRNA counts: i) 'partially resistant' - gRNA<100; 'permissive' - 100<gRNA<10^5; 'super-permissive' - gRNA>10^5. The total gRNA within the infected wells was obtained by summing gRNA counts in population and the figure shows the relative fraction from each classification. Representative max-projected images of cells in each category are shown. (2-8 hpi, n≥3; 10 and 24 hpi, n=2)

(E) Identification of super-permissive cells from a low-magnification (20x) high-throughput smFISH assay (left panels). Full z-projected (9 μm) images of infected Vero E6 cells hybridised with +ORF1a probes are shown. At this magnification, only the cells with vRNA count > ~105 (i.e., corresponding to 'super-permissive' cells) exhibit significant smFISH fluorescence compared to uninfected cells. Scale bar = 250 μm. Percentage of super-permissive cells in untreated and RDV-treated conditions at 8 and 24 hpi (right panel). Labels represent average values. Data represented as mean ± S.D. (n=3, ~ 2000 cells were scanned from each replicate well). Student's t-test. ***, p<0.001; ****, p<0.0001.

(F) Percentage of infected cells expressing sgRNA. sgRNA expressing cells were identified by those having an (ORF-N – ORF1a) probe count more than 1. Data represented as mean ± S.E. (2-8 hpi, n≥3; 10 and 24 hpi, n=2).

(G) Per cell ratio of sgRNA/gRNA counts across the time series. Gray symbols represent cell-to-cell median values whereas the line plot represents ratio calculated from population sum of gRNA and sgRNA. The number of cells analysed are the same as in (Figure 3C), with the exception of cells having equal ORF1a and ORF-N probe counts. Horizontal dashed line represents value of 1. (2-8 hpi, n≥3; 10 and 24 hpi, n=2).

(H) Per cell ratio of sgRNA/gRNA counts grouped by gRNA burden classification as in (Figure 3D). Data represents median ± S.E. Horizontal dashed line represents value of 1. (2-8 hpi, n≥3; 10 and 24 hpi, n=2).

(I) The number of viral factories per cell increase over time as assessed by smFISH cluster detection. Cells harbouring > 107 copies of RNA, less than 10 molecules of RNA, cells with no viral factories, and cells from 24 hpi timepoints were excluded from this analysis. Data represented as mean ± S.E. Number of cells analysed (Untreated/RDV): 2 hpi, 494/240; 4 hpi, 758/494; 6 hpi, 315/417; 8 hpi, 933/877; 10 hpi, 726/885. (2-8 hpi, n≥3; 10 and 24 hpi, n=2).

(J) The kinetics of gRNA copies within viral factories. Spatially extended viral factories were resolved by cluster decomposition to obtain single-molecule counts. The type and number of cells analysed are the same as in (Figure 3I). (2-8 hpi, n≥3; 10 and 24 hpi, n=2).

Figure S3. The dynamics and heterogeneity of SARS-CoV-2 RNA replication.

(A) Dose response curve of remdesivir (RDV) versus SARS-CoV-2 RNA replication. Viral RNA was quantified using RT-qPCR in infected Vero E6 cells, targeting the ORF-N region. IC50 and IC90 values were estimated by fitting a nonlinear (weighted) least-squares model on the data (n=3).

(B) Experimental design to profile SARS-CoV-2 replication kinetics in late-stage infection. Vero E6 cells were seeded on cover-glass and 24 h later, inoculated with SARS-CoV-2 (Victoria strain, MOI = 1) for 2 h. Non-internalised viruses were removed by trypsin digestion and cells were fixed at timepoints shown for hybridisation with +ORF1a probe. In remdesivir (RDV) condition, the drug (10 μM) was added to cells at 24 hpi and maintained for the times shown.

(C) Representative full z-projected confocal images of infected cells from the time series. Viral gRNA was visualised with +ORF1a probes. Images were contrasted to equivalent single molecule intensity. Scale bar = 20 μm.

(D) Quantification of viral gRNA counts in untreated and RDV treated cells. Reference RNA intensity was acquired with Bigfish from less dense region of the images. Viral gRNA counts

were quantified by extrapolating single-molecule intensity over total cellular integrated intensity. Data represented as median ± S.E. (n=2).

(E) The number of viable cells per field of view across the time series. Viable cells were quantified by counting non-condensed nuclei in randomly sampled field of views from (Figure S3C). Non-condensed nuclei counts were normalised to the average count values from uninfected 'Mock' condition. Student's t-test. ****, $p<0.0001$. Data represented as mean ± S.E. (n=2).

Figure 4. Heterogeneous SARS-CoV-2 RNA replication.

(A) Representative 60x magnified field of view (FOV) of SARS-CoV-2 infected Vero E6 cells at 8 hpi (Victoria strain, MOI = 1). smFISH against ORF1a was used to visualise cellular heterogeneity in viral RNA counts. Magnified panels show (i) a 'super-permissive' cell, and (ii) a cell with discrete viral RNA copies. Scale bar = 10 or 50 µm.

(B) Discrete separation of gRNA count distribution among infected cells randomly sampled at 8 hpi, where each dot symbol represents a cell. Statistics for the percentage of infected cells and frequency of 'super-permissive' cells at 8 hpi. Quantification was performed per field of view and the number labels represent average values. Cells with > 10^5 gRNA copies were considered to be 'super-permissive', as classified as 'High' in (Figure S3C-D) (gRNA quantification: n=4, 148 uninfected and 316 infected cells; Percentage infection: n=3).

(C-D) Heterogeneous SARS-CoV-2 replication in lung epithelial A549-ACE2 and Calu-3 cells. The percentage of infected and super-permissive cells were quantified as with Vero E6 cells above. Scale bar = 50 µm (A549-ACE2, n=2; Calu-3, n=3).

(E-F) Spatial distribution analysis of super-permissive Vero E6 and A549-ACE2 cells at 8 hpi. Low magnification smFISH overview of infected cells (top left). 2D mask of super-permissive cells (top right). An example of randomly simulated points within the DAPI mask (bottom left). Same number of random points as super-permissive cells were simulated 10 times per FOV. Histogram of nearest neighbour distances calculated from super-permissive cells (Observed) and randomly simulated points (Random) (bottom right). Further modes of spatial analyses are presented in (Figure S4) with infected Calu-3 cells. All confocal images are presented as maximum full z-projection. Data represented as mean ± S.D. Student's t-test. p-values are shown on the presented visual. (Vero E6, n=3; A549-ACE2, n=2)

Figure S4. Spatial distribution of super-permissive SARS-CoV-2 infected cells.

Spatial distribution analysis of super-permissive SARS-CoV-2 (Victoria strain) infected Calu-3 cells. Cells were infected with SARS-CoV-2 (Victoria strain) at an MOI of 1, fixed at 8 hpi and hybridised with +ORF1a smFISH probe to visualise viral RNA.

(A) Low magnification image (full z-projection) of infected Calu-3 cells showing a small population of super-permissive cells visible with smFISH. Scale bar = 250 µm.

(B) 2D mask generated from spatial coordinates of super-permissive cells.

(C) Observed distribution of super-permissive cells (Data) and example coordinates of the three modes of spatial distributions: i) evenly spaced, ii) clustered and iii) random. The simulations were confined to DAPI positive areas.

(D) Density plot of nearest neighbour distances obtained from the spatial distribution analysis. Each mode of simulations was iterated 10 times per image.

(E) Beeswarm plot of nearest neighbour distances obtained from the spatial distribution analysis. One-way ANOVA with post-hoc Tukey test. (n=3).

Figure 5. Delayed replication kinetics of B.1.1.7 variant.

(A) Experimental design to compare the replication kinetics of Victoria and B.1.1.7 SARS-CoV-2 strains. Vero E6 cells were seeded on cover-glass and 24 h later, inoculated with Victoria or B.1.1.7 strain (MOI = 1) for 2 h. Non-internalised viruses were removed by trypsin digestion and cells were fixed at designated timepoints for hybridisation with +ORF1a and +ORF-N probes. In remdesivir (RDV) condition, the drug was added to cells at 10 µM during virus inoculation and maintained for the infection period.

(B) Maximum z-projected confocal images of Vero E6 cells infected with Victoria or B.1.1.7 strains. Representative super-permissive cells from the time series are shown. Scale bar = 10 µm.

(C) Comparing viral gRNA counts at 2 hpi between Victoria and B.1.1.7. Each symbol represents a cell. Different hue of colours represents readings taken from individual repeat experiments, and the labels represent average values. (n=3; Victoria, 424 cells; B.1.1.7, 519 cells). Mann-Whitney U test.

(D) Comparing percentage of infected cells between the two viral strains at 2 hpi. Infected cells were determined by +ORF1a smFISH fluorescence. Data represents mean ± S.D. (n=3). Student's t-test.

(E) Bigfish quantification of +ORF1a and +ORF-N smFISH counts per cell. Due to bimodality of the data, statistical significance was determined using two-sample Kolmogorov-Smirnov test to compare cumulative distribution of +ORF1a counts between the two strains. (n=3). (Victoria, 2 : 6 : 8 hpi = 424 : 558 : 482 cells; B.1.1.7, 2 : 6 : 8 hpi = 519 : 465 : 503 cells). n.s., not significant; *, p<0.5: ***, p<0.001; ***, p<0.0001.

(F) Comparing the number of viral factories per cell between the two viral strain across the time series. Viral factories were identified using Bigfish cluster detection as with (Figure 3E). Data represented as mean ± S.E. (n=3).

(G) Density ridge plot showing the number of gRNA copies within viral factories for Victoria and B.1.1.7 variants. The density distribution represents the number of molecules per viral factories per cell. Vertical segment symbol represents a cell. (n=3).

(H) Comparison of the percentage of super-permissive cells between the two strains assessed from low-magnification high-throughput smFISH assay (see (Figure S5A-B) for details). Data represented as mean ± S.D. (n=3). n.s., not significant; ***, p<0.001; ****, p<0.0001.

Figure S5. Delayed replication kinetics of B.1.1.7 SARS-CoV-2 variant.

(A) Low-magnification (20x) z-projected (6 µm) images of +ORF1a & +ORF-N smFISH in infected Vero E6 cells. Cells were seeded on cover-glass and 24 h later, inoculated with Victoria or B.1.1.7 strain (MOI = 1) for 2 h. Non-internalised viruses were removed by trypsin digestion and cells were fixed at designated timepoints. In remdesivir (RDV) condition, the drug was added to cells at 10 µM during virus inoculation and maintained for the infection period. Scale bar = 250 µm.

(B) Scatter plot showing high-throughput smFISH intensity quantification of +ORF1a & +ORF-N in Victoria and B.1.1.7 infected cells. Each symbol represents a cell. Fluorescence density was measured from 20x overview scans of approximately ~ 60% of the culture well area. At this magnification, smFISH fluorescence is only detectable in 'super-permissive' cells (>105 vRNA). Percentage of super-permissive cells were calculated based on a gate set with +ORF-N signal using uninfected (Mock) condition signal as a threshold (vertical line) (n=3).

(C) Spatial distribution analysis of B.1.1.7 infected Vero E6 cells showing super-permissive phenotype. Low magnification smFISH overview of infected cells (top left). 2D mask of super-permissive cells (top right). An example of randomly simulated points within the DAPI mask (bottom left). Same number of random points as super-permissive cells were simulated 10 times per FOV. Histogram of nearest neighbour distances calculated from super-permissive cells (Observed) and randomly simulated points (Random) (bottom right). (n=2).

Figure 6. Transcriptomic landscape of B.1.1.7 and Victoria SARS-CoV-2 strains.

(A) Experimental design to compare replication kinetics and transcriptomic landscapes of Victoria and B.1.1.7 strains. A549-ACE2 cells were seeded and 24 h later, inoculated with Victoria or B.1.1.7 strain (MOI = 1) for 2 h. Non-internalised viruses were removed by trypsin digestion and cells were fixed at designated timepoints for smFISH or harvested for RNA-seq library preparation.

(B) Maximum z-projected confocal images of A549-ACE2 cells infected with Victoria or B.1.1.7. Representative super-permissive cells from the time series are shown. Numbers at the bottom left corner indicate dynamic contrast range used to display the image. Scale bar = 10 µm.

(C) Comparison of the percentage of super-permissive cells between the two strains. Super-permissive cells were identified from low-magnification high-throughput smFISH assay (see Figure 7SB-C). Data represented as mean ± S.D. (8 hpi n=2; 24 hpi n=3). *, p<0.5: **, p<0.01.

(D) Read coverage along SARS-CoV-2 genome (positive strand) for the two variants in the three timepoints. Counts are normalised to total read count to show the increased proportion of reads from the virus in addition to the accumulation of sub-genomic RNA, and averaged across replicates. (n=3).

(E) Percentage of reads mapping to SARS-CoV-2 genome of total mapped reads, shown separately for the two strains. Each symbol represents an experimental replicate. (n=3).

(F) Percent of reads mapping to SARS-CoV-2 negative (antisense) strand relative to all SARS-CoV-2 reads, shown separately for the two strains. Each symbol represents an experimental replicate (n=3).

(G) Estimated ratio of SARS-CoV-2 sub-genomic to genomic RNA for the two virus variants at the three timepoints. Student's t-test. n.s., not significant; * , p<0.05; ****, p<0.001. (n=3).

Figure S6. Transcriptomic landscapes of B.1.1.7 and Victoria and SARS-CoV-2 strains.

This figure supplements the presented visuals in (Figure 7). A549-ACE2 cells were seeded and 24 h later, inoculated with Victoria or B.1.1.7 strain (MOI = 1) for 2 h. Non-internalised viruses were removed by trypsin digestion and cells were fixed at designated timepoints for smFISH or harvested for RNA-seq library preparation.

(A) Comparing percentage of infected A549-ACE2 cells between Victoria and B.1.1.7 at 2 hpi (left). Infected cells were determined by +ORF1a smFISH fluorescence. Data represented as mean ± S.D. Comparison of viral gRNA counts at 2 hpi between the two variants (right). Each dot represents a cell. Data represented as mean ± S.E. and the labels represent average values.

(B) Low-magnification z-projected (9 µm) images of SARS-CoV-2 infected A549-ACE2 cells. Cells were hybridised with ORF1a & ORF-N probes to visualise super-permissive cells. Scale bar = 500 µm.

(C) Scatter plot showing high-throughput smFISH intensity quantification of ORF1a & ORF-N probes in infected cells. Each dot is a cell. Fluorescence signal density was measured from low-magnification overview image of entire culture wells. A gate was set with ORF-N signal using uninfected condition to threshold percentage of super-permissive cells (dotted line) (2-4 hpi, n=2; 24 hpi, n=3).

(D) First two components of a principal component analysis (PCA) performed on the 500 host genes showing the highest variance in RNA-seq. The infection timepoints (coloured) and control (gray) samples group into separate clusters but the samples the two strains remain close to one another. (n=3).

STAR★Methods

Cell culture. Vero E6, A549-ACE2 (kind gift from Bartenschlager lab) (Klein et al., 2020) and Huh-7.5 cells were maintained in standard DMEM, Calu-3 cells in Advanced DMEM both supplemented with 10% fetal bovine serum, 2mM L-glutamine, 100 U/mL penicillin and 10µg/mL streptomycin and non-essential amino acids. All cell lines were maintained at 37oC and 5% CO2 in a standard culture incubator.

Virus propagation and infection. SARS-CoV-2 strains: Victoria 01/20 (BVIC01) (Caly et al., 2020) (provided by PHE Porton Down after supply from the Doherty Centre Melbourne, Australia) and B.1.1.7 (Tegally et al., 2020) (20I/501Y.V1.HMPP1) (provided by PHE Porton Down). Viral strains were propagated in Vero-E6 cells as described (Wing et al., 2021). Briefly, naïve Vero E6 cells were infected with SARS-CoV-2 at an multiplicity of infection (MOI) of 0.003 and incubated for 48-72h until visible cytopathic effect was observed. At this point, cultures were harvested, clarified by centrifugation to remove residual cell debris and stored at -80oC. To determine the viral titre, fresh Vero E6 cells were inoculated with serial dilutions of SARS-CoV-2 viral stocks for 2h followed by addition of a semi-solid overlay consisting of 1.5% carboxymethyl cellulose (SIGMA). Cells were incubated for 72h and visible plaques enumerated by fixing cells using amido black stain to calculate plaque-forming units (PFU) per ml. Similarly, HCoV-229E (Andrew Davidson lab (Bristol) and Peter Simmmonds lab (Oxford)) virus was propagated in Vero E6 cells and TCID50 was performed in Huh-7.5 cells.

For smFISH experiments with the SARS-CoV-2 stains, cells were infected at an MOI of 1 for 2h followed by extensive washing in PBS. Residual cell surface associated virus was removed by trypsin treatment of the cell monolayer for 2mins followed by neutralisation of the trypsin using serum containing media. Infected cells were then maintained for defined periods up to 24h. For the HCoV-229E, cells were infected at an MOI of 1 and were maintained for 24 and 48h.

RT-qPCR. Infected cells were harvested in RLT buffer and RNA extracted using the Qiagen RNAeasy kit. SARS-CoV-2 RNA was quantified using a one-step reverse transcriptase qPCR (RT-qPCR) kit (Takyon) in a multiplexed reaction containing primer probes directed against the SARS-CoV-2 N gene (FAM) and ß-2-Microglobulin (VIC) as an internal control. All qPCR reactions were carried out using a Roche 96 Light cycler (Roche). (SARS primer probe IDT CAT:100006770, B2M primer probe Applied Biosystems 4325797)

Single molecule fluorescence in situ hybridisation (smFISH). smFISH was carried out as previously reported (Titlow et al., 2018; Yang et al., 2017) with minor modifications. Briefly, cells were grown on #1.5 round glass coverslips in 24-well plate or in µ-Slides 8 well glass bottom (IBIDI) and fixed in 4% paraformaldehyde (Thermo Fisher) for 30 min at room temperature. Cells were permeabilised in PBS/0.1% Triton X-100 for 10 min at room temperature followed by washes in PBS and 2x SSC. Cells were pre-hybridised in pre-warmed (37˚C) wash solution (2x SSC, 10% formamide) twice for 20 min each at 37˚C. Hybridisation was carried out in hybridisation solution (2x SSC, 10% formamide, 10% dextran sulphate) containing 500 nM smFISH probes overnight at 37˚C. For infection timepoints beyond 24 h, smFISH probes were added at 1 µM. After the overnight hybridisation, cells were washed for 20 min in pre-warmed wash solution at 37˚C followed by counterstain with DAPI (1 µg/ml), phalloidin-Alexa Fluor 488 conjugate (264 nM) and/or CellMask Green (1:1,000,000) diluted in wash solution. Cells were then washed once with wash solution for 20 min at 37˚C and twice with 2x SSC for 10 min each at room temperature. Cells were mounted using Vectashield, IBIDI mounting media or 2x SSC.

For RNase digestion experiments, RNaseT1 (Thermo Fisher, EN0541, 100 U/ml) or RNaseIII (M0245S, NEB, 20 U/ml) was used to degrade single-stranded RNA and double-stranded RNA, respectively. Permeabilised cells were treated with RNases in PBS supplemented with 5 mM MgCl2 and incubated at 37˚C for 1 h and washed three times with PBS.

In the experiment to detect viral negative strands, double-stranded RNA (dsRNA) was denatured using DMSO, formamide or NaOH. After the permeabilisation step, cells were rinsed in distilled water and were treated with 50 mM NaOH for 30s at room temperature, 70% formamide at 70˚C for 1 h or 90% DMSO at 70˚C for 1 h. Following the treatments, cells were quickly cooled on ice, washed in ice-cold PBS and subjected to standard smFISH protocol.

smFISH probe design and specificity analysis. Candidate smFISH probe sequences were acquired using Stellaris® Probe Designer version 4.2 (https://www.biosearchtech.com/stellaris-designer) with following parameters: Organism – Human, Masking level – 5, Oligo length – 20 nt, Minimum spacing length – 3 nt. Appropriate region of the SARS-CoV-2 Wuhan-Hu-1 (NC_045512.2) reference sequence was used as target sequence. Candidate sequences were BLAST screened against custom human transcriptome and intron database to score number of off-target base-pair matches, then 35 – 48 sequences with the least match scores were chosen per probe set. Oligonucleotides were singly labelled with ATTO633, ATTO565, Cy3, or ATTO488 at 3' ends according to a

published protocol (Gaspar et al., 2017) and were concentration normalised to 25 µM. All probe sets used in this study had degree of labelling > 0.94.

For in silico probe sequence specificity analysis, selected oligonucleotide sequences were aligned against SARS-CoV-1 (NC_004718), SARS-CoV-2 (NC_045512), MERS-CoV (NC_019843), HCoV-229E (NC_002645), HCoV-NL63 (NC_005831), HCoV-OC43 (NC_006213), HCoV-HKU1 (NC_006577), Human (GCF_000001405.39), and African green monkey (GCF_015252025.1) RefSeq genome or transcriptome assembly using 'bowtie2' (2.4.4) (Langmead and Salzberg, 2012). Following bowtie2 arguments were used to find minimum edit distance of oligonucleotide sequences to target genome/transcriptome: --end-to-end --no-unal --align-seed-mm 0, --align-seed-length 5, --align-seed-interval 1-1.15, --effort-extend 15, --effort-repeat 2. Melting temperatures were obtained using 'rmelting' (1.8.0) R package at 300mM Na concentration (2x SSC). smFISH probe sequences used in this study are available in supplementary files.

Immunofluorescence. After permeabilisation, cells were blocked in blocking solution (50% Li-Cor Odyssey blocking solution, pretreated with RNASecure for 30 min and supplemented with 2 mM ribonucleoside vanadyl complex and 0.1% Tween-20) for 30 min at room temperature. Then, cells were incubated with J2 primary antibody (Scicons 10010200) at 0.5 µg/ml or human anti-N primary antibody (Ey2B clone 1:2000) (Huang et al., 2020) for 2 h at room temperature. Cells were washed three times in PBS/ 0.1% Tween-20 (PBSTw) for 10 min each at room temperature and incubated with fluorescent secondary antibodies (1:500) diluted in blocking solution for 1 h at room temperature. After further three washes in PBSTw, cells were mounted using Vectashield or IBIDI mounting media. For combined smFISH and immunofluorescence, antibody staining was carried out sequentially after the smFISH protocol.

Microscopy and image handling. Cells were images on an Olympus SpinSR10 spinning disk confocal system equipped with Prime BSI and Prime 95B sCMOS cameras. Objectives used were 20x dry (0.8 NA, UPLXAPO20X), 60x silicone oil (1.3 NA, UPLSAPO60XS2), 60x oil (1.5 NA, UPLAPOHR60X), or 100x oil (1.45 NA, UPLXAPO100XO). Image voxel sizes were 0.55 x 0.55 x 2 µm (x:y:z) with the 20x objective and 0.11 x 0.11 x 0.2 µm (x:y:z) with the 60x and 100x objectives. Automatic and manual image acquisition and image stitching were performed with Olympus cellSens Dimension software. Images were uploaded and stored in

the University of Oxford OMERO server (Allan et al., 2012) and OMERO.figure (3.2.0) was used to generate presented image visualisations.

Image analysis

Cell segmentation and counting. Cell segmentation was performed either manually in ImageJ (National Institute of Health) or automatically with Cellpose (0.6.1) (Stringer et al., 2021) using 2D maximum intensity projected images of phalloidin or CellMask stains. Cellpose parameters for 60x and 100x magnification images were model_type=cyto, diameter=375, flow_threshold=0.9, cellprob_threshold=-3. For 20x stitched images, CellMask channel was deconvolved with constrained iterative module using cellSens (5 iterations, default spinning disk PSF, Olympus), then following Cellpose parameters were used: model_type=cyto, diameter=55, flow_threshold=0, cellprob_threshold=-6. Total number of cells per image was counted using a custom ImageJ macro script or from the Cellpose segmentation output on DAPI channel images (model_type=nuclei, diameter=20, default threshold). Infected cells were counted using ImageJ "3D object counter" or manually.

Quantification of smFISH images. Single-molecule level quantification of smFISH images were performed either with FISH-quant (Mueller et al., 2013) or Bigfish (https://github.com/fish-quant/big-fish). For FISH-quant, ImageJ ROI files were converted to FQ outline file using a custom python script. Then, smFISH channels were Laplacian of Gaussian filtered (sigma = 7, 3 px) and pre-detected using local maximum mode with "allow smaller z region for analysis" option enabled. Pre-detected diffraction limited spots were fitted with 3D Gaussian and thresholded in batch mode based on filtered intensity, amplitude and σz. Thresholds were defined by uninfected "Mock" condition samples. Viral factories were quantified using the TxSite quantification mode of FISH-quant (xy:z = 500:1200 nm crop per factory) with normal-sampled averaged single-molecule image (xy:z = 15:12 px) from batch mode output by integrated intensity in 3D method. Similarly, cells displaying high viral load were quantified by analogously integrating smFISH intensities, subtracting uninfected condition background fluorescence and dividing by the intensity of reference single-molecules.

Large smFISH datasets were processed with a custom python pipeline using Bigfish, skimage, and numpy libraries (available in the Github repository). Tif files were converted to a numpy array and individual cells were segmented from the image using the Cellpose library as described above. Images where cells were labelled with the CellMask stain were pre-processed with a median filter, radius = 50. Background signal in the smFISH channel was subtracted with the skimage.white_tophat algorithm (radius = 5, individual z frames were

processed in 2D due to memory constraints, results were indistinguishable from 3D-processed images). Threshold setting for smFISH spot detection was set specifically for each set of images collected in each session. Viral factories were resolved using `decompose_cluster()` function to find a reference single-molecule spot in a less signal-dense region of the image, which was used to simulate fitting of the gaussian modelised reference spot into viral factories until the local signal intensities were matched. Decomposed spots were grouped into clusters with previously reported radii of double-membrane vesicles (DMV) measured by electron microscopy (150nm pre-8hpi and 200nm post-8hpi) (Cortese et al., 2020).

Dual colour smFISH spot detection analysis. The same viral RNA target was detected using two smFISH probes labelled with alternating (ODD and EVEN) red and far-red fluorochromes. Resulting images were processed in FISH-quant to obtain 3D coordinates of each spots. Percentage co-localisation analysis was performed with a custom script using an R package "FNN" (1.1.3). Briefly, we calculated 3D distance of nearest neighbour for each spot in the red channel to the closest detected spot in the other channel and repeated the analysis starting from the far-red channel. We then used a value of 300 nm to define co-localised spots corresponding to the same viral RNA molecule. The presented visuals report percentage co-localisations calculated from the red channel to the far-red channel and vice-versa. The analysis was performed per field of view.

Quantification of fluorescence intensity and signal colocalization. Immunofluorescence images were background subtracted using rolling ball subtraction method (radius = 150 px) in ImageJ. Anti-dsRNA (J2) stain was quantified by integrating fluorescence signal across the z-stacks of cellular region of interest divided by the cell volume to obtain signal density. Signal density was normalised to the average signal density of uninfected "Mock" condition cells. Fluorescence intensity profiles were obtained using ImageJ "plot profile" tool across 3 µm region on 1 µm maximum intensity projected images. To assess colocalisation of N protein with SARS-CoV-2 RNA, ellipsoid mask centred around centroid xyz coordinates of smFISH spots were generated with the size of the point-spread function (xy radius=65 nm, z radius=150 nm) using ImageJ 3D suite. Integrated density of N-protein channel (background subtracted, radius=5px) fluorescence within the ellipsoid mask was measured and compared to the equivalent signal in the uninfected condition.

Simulation of highly permissive cell distribution. Simulations were performed to determine if Covid19 superinfection follows a random distribution. The general strategy was to test the

complete spatial randomness hypothesis by comparing the average nearest neighbour distance of superinfected cells to an equal number of randomly selected coordinates (Ripley, 1979). 2D spatial coordinates of superinfected cells were obtained from the 3D-obect counter (ImageJ) as described above. Cell nuclei were segmented with the DAPI channel and placement of random coordinates was confined to pixels that fell within the DAPI segmentation mask. Nearest neighbour distances were calculated using the KDtree algorithm (Maneewongvatana and Mount, 1999) implemented in python (scipy.spatial.KDTree). Pseudo-random distributions were simulated by randomly placing the first coordinate, then constraining the placement of subsequent coordinates to within a defined number of pixels.

RNA-sequencing library preparation. RNA from infected cells were extracted as described above. Sequencing libraries were prepared using the Illumina Total RNA Prep with Ribo-Zero Plus library kit (Cat# 20040525) according to manufacturer's guidelines. Briefly, 100ng of total RNA was first depleted of the abundant ribosomal RNA present in the samples by rRNA targeted DNA probe capture followed by enzymatic digestion. Samples were then purified by Beckman Coulter RNAClean XP beads (Cat #A63987). Obtained rRNA-depleted RNA was fragmented, reverse transcribed, converted to dsDNA, end repaired and A-tailed. The A-tailed DNA fragments were ligated to anchors allowing for PCR amplification with Illumina unique dual indexing primers (Cat#20040553). Libraries were pooled in equimolar concentrations and sequenced on Illumina NextSeq 500 and NextSeq 550 sequencers using high-output cartridges (Cat# 20024907), generating single 150nt long reads.

RNA-sequencing analysis

Genomes. We downloaded the human genome primary assembly and annotation from ENSEMBL (GRCh38.99) and the SARS-CoV-2 RefSeq reference genome from NCBI (NC_045512.2). We combined the human and viral genome and annotation files into one composite genome and annotation file for downstream analyses.

Alignment and gene counts. We performed a splice-site aware mapping of the sequencing reads to the combined human and SARS-CoV-2 genome and annotation using STAR aligner (2.7.3a) (Dobin et al. 2013). We also used STAR to assign uniquely mapping reads in strand-specific fashion to the ENSEMBL human gene annotation and the two SARS-CoV-2 strands.

Principal Component Analysis. To assess if SARS2 infection is the main driver of differences in the RNA-seq samples, we performed a principal component analysis (PCA). First, we performed library size correction and variance stabilisation with regularized–

logarithm transformation implemented in DESeq2 (1.28.1) (Love et al. 2014). This corrects for the fact that in RNA-seq data, variance grows with the mean and therefore, without suitable correction, only the most highly expressed genes drive the clustering. We then used the 500 genes showing the highest variance to perform PCA using the prcomp function implemented in the base R package stats (4.0.2) (R Core Team 2020).

SARS-CoV-2 sub-genomic RNA expression. To assess relative levels of viral sub-genomic and genomic RNA expression, we tallied the alignments (using GenomicRanges and GenomicAlignments R packages (Lawrence et al., 2013)) mapping to the region unique to the genomic RNA and the shared region and normalised for their respective lengths. Unique contribution of sgRNA region was then estimated by subtracting the contribution of the genomic RNA from the shared region. To avoid spurious mappings, we filtered for skip sites that were present in all three replicates and constituted at least 0.1% of all skipped viral reads.

Statistics, data wrangling and visualisation. Statistical analyses were performed in R (3.6.3) and RStudio (1.4) environment using an R package “rstatix” (0.7.0). P values were adjusted using the Bonferroni method for multiple comparisons. The “tidyverse suite” (1.3.0) was used in R, and “Numpy” and “Pandas” python packages were used in Jupyter notebook for data wrangling. Following R packages were used to create the presented visualisation: “ggplot2” (3.3.2), “ggbeeswarm” (0.6.0), “hrbrthemes” (0.8.0), “scales” (1.1.1), and “patchwork” (1.1.1). Further visual annotations were made in the Affinity Designer (Serif).

Author contributions

J.Y.L. designed and conducted experiments, designed and carried out quantitative image and bioinformatic analysis pipelines, drafted the figures and co-wrote the manuscript. P.A.C.W designed and conducted experiments, co-revised the manuscript. D.S.G. Conducted experiments and quantitative image analysis and A.J. A.J. designed and carried out bioinformatics and next-generation sequencing analysis**.** J.T. designed and conducted quantitative image analysis of viral RNA numbers and distribution**,** M.N. Carried out experiments (in Category III Containment labs). X.Z. Carried out experiments (in Category III Containment labs)**,** N.J. Carried out sequencing experiments (on infection time courses of variants). L.I. provided resources (Coronavirus strain causing human cold). M.K.T. designed and wrote quantitative software for viral RNA stability, R.M.P. provided advice and discussion for advanced microscopy performace and image analysis, A.W. provided resources (Setup bespoke microscopes and labs for this project, and quality control of microscope

performance). D.D.A. Provided discussion of the design of the experiments and their interpretation. W.J. Provided resources (the Alpha variant and facilitated the extensive and complex Containment Category III work at the Dunn School of Pathology). A.C. co-designed the study, the bioinformatics analysis methods and co-wrote the manuscript. J.A.M. co-designed the study and co-wrote the manuscript. I.D. co-designed the study, the computational methods for quantitative analysis of virus numbers, single cell analysis and spatial distributions, and co-wrote the manuscript.

Declaration of interests

The authors have no relevant interests to declare.

Acknowledgements

We are grateful to Danail Stoychev and Maria Kiourlappou for the advice on Python programming and high-performance computing. We are very grateful to Olympus UK and Europe for their generous loan of an Olympus IXplore SpinSR spinning disk system for the imaging work in this project and to Matthew Freeman and Jordan Raff for enabling us to install the microscope in the Dunn School of Pathology specifically for this SARS-CoV-2 work.

Funding

I.D. The Davis laboratory is funded by Wellcome IA 209412/Z/17/Z and Wellcome Strategic Awards 091911/B/10/Z and 107457/Z/15/Z. J.Y.L. D.G.S. is funded by the Medial Sciences Graduate Studentship, University of Oxford. M.K.T. is funded by a Leverhulmne Grant to I.D. J.A.M. The McKeating laboratory is funded by a Wellcome Investigator Award (IA) 200838/Z/16/Z, UK Medical Research Council (MRC) project grant MR/R022011/1, and the Chinese Academy of Medical Sciences (CAMS) Innovation Fund for Medical Science (CIFMS), China (grant number: 2018-I2M-2-002). A.C. is supported by an MRC Career Development Award (MR/L019434/1), MRC grants (MR/R021562/1, MC_UU_12014/10, and MC_UU_12014/12), and John Fell funds, University of Oxford.

References

Alexandersen, S., Chamings, A., and Bhatta, T.R. (2020). SARS-CoV-2 genomic and subgenomic RNAs in diagnostic samples are not an indicator of active replication. Nat Commun *11*, 6059.

Allan, C., Burel, J.M., Moore, J., Blackburn, C., Linkert, M., Loynton, S., Macdonald, D., Moore, W.J., Neves, C., Patterson, A.*, et al.* (2012). OMERO: flexible, model-driven data management for experimental biology. Nat Methods *9*, 245-253.

Appelberg, S., Gupta, S., Svensson Akusjarvi, S., Ambikan, A.T., Mikaeloff, F., Saccon, E., Vegvari, A., Benfeitas, R., Sperk, M., Stahlberg, M.*, et al.* (2020). Dysregulation in Akt/mTOR/HIF-1 signaling identified by proteo-transcriptomics of SARS-CoV-2 infected cells. Emerg Microbes Infect *9*, 1748-1760.

Belkowski, L.S., and Sen, G.C. (1987). Inhibition of vesicular stomatitis viral mRNA synthesis by interferons. J Virol *61*, 653-660.

Best Rocha, A., Stroberg, E., Barton, L.M., Duval, E.J., Mukhopadhyay, S., Yarid, N., Caza, T., Wilson, J.D., Kenan, D.J., Kuperman, M.*, et al.* (2020). Detection of SARS-CoV-2 in formalin-fixed paraffin-embedded tissue sections using commercially available reagents. Lab Invest *100*, 1485-1489.

Billman, M.R., Rueda, D., and Bangham, C.R.M. (2017). Single-cell heterogeneity and cell-cycle-related viral gene bursts in the human leukaemia virus HTLV-1. Wellcome Open Res *2*, 87.

Boersma, S., Rabouw, H.H., Bruurs, L.J.M., Pavlovic, T., van Vliet, A.L.W., Beumer, J., Clevers, H., van Kuppeveld, F.J.M., and Tanenbaum, M.E. (2020). Translation and Replication Dynamics of Single RNA Viruses. Cell *183*, 1930-1945 e1923.

Burgess, H.M., and Mohr, I. (2015). Cellular 5'-3' mRNA exonuclease Xrn1 controls double-stranded RNA accumulation and anti-viral responses. Cell Host Microbe *17*, 332-344.

Burke, J.M., St Clair, L.A., Perera, R., and Parker, R. (2021). Rapid decay of host basal mRNAs during SARS-CoV-2 infection perturbs host antiviral mRNA biogenesis and export. bioRxiv, 2021.2004.2019.440452.

Caly, L., Druce, J., Roberts, J., Bond, K., Tran, T., Kostecki, R., Yoga, Y., Naughton, W., Taiaroa, G., Seemann, T.*, et al.* (2020). Isolation and rapid sharing of the 2019 novel coronavirus (SARS-CoV-2) from the first patient diagnosed with COVID-19 in Australia. Med J Aust *212*, 459-462.

Cao, Y., Xu, X., Kitanovski, S., Song, L., Wang, J., Hao, P., and Hoffmann, D. (2021). Comprehensive Comparison of RNA-Seq Data of SARS-CoV-2, SARS-CoV and MERS-CoV Infections: Alternative Entry Routes and Innate Immune Responses. Front Immunol *12*, 656433.

Carlson, C.R., Asfaha, J.B., Ghent, C.M., Howard, C.J., Hartooni, N., Safari, M., Frankel, A.D., and Morgan, D.O. (2020). Phosphoregulation of Phase Separation by the SARS-CoV-2 N Protein Suggests a Biophysical Basis for its Dual Functions. Mol Cell *80*, 1092-1103 e1094.

Carossino, M., Ip, H.S., Richt, J.A., Shultz, K., Harper, K., Loynachan, A.T., Del Piero, F., and Balasuriya, U.B.R. (2020). Detection of SARS-CoV-2 by RNAscope((R)) in situ hybridization and immunohistochemistry techniques. Arch Virol *165*, 2373-2377.

Chen, J., Wang, R., Wang, M., and Wei, G.W. (2020). Mutations Strengthened SARS-CoV-2 Infectivity. J Mol Biol *432*, 5212-5226.

Chou, Y.Y., and Lionnet, T. (2018). Single-Molecule Sensitivity RNA FISH Analysis of Influenza Virus Genome Trafficking. Methods Mol Biol *1836*, 195-211.

Chu, H., Chan, J.F., Yuen, T.T., Shuai, H., Yuan, S., Wang, Y., Hu, B., Yip, C.C., Tsang, J.O., Huang, X.*, et al.* (2020). Comparative tropism, replication kinetics, and cell damage profiling of SARS-CoV-2

and SARS-CoV with implications for clinical manifestations, transmissibility, and laboratory studies of COVID-19: an observational study. Lancet Microbe *1*, e14-e23.

Collier, D.A., De Marco, A., Ferreira, I., Meng, B., Datir, R.P., Walls, A.C., Kemp, S.A., Bassi, J., Pinto, D., Silacci-Fregni, C.*, et al.* (2021). Sensitivity of SARS-CoV-2 B.1.1.7 to mRNA vaccine-elicited antibodies. Nature *593*, 136-141.

Cortese, M., Lee, J.Y., Cerikan, B., Neufeldt, C.J., Oorschot, V.M.J., Kohrer, S., Hennies, J., Schieber, N.L., Ronchi, P., Mizzon, G.*, et al.* (2020). Integrative Imaging Reveals SARS-CoV-2-Induced Reshaping of Subcellular Morphologies. Cell Host Microbe *28*, 853-866 e855.

Davies, N.G., Abbott, S., Barnard, R.C., Jarvis, C.I., Kucharski, A.J., Munday, J.D., Pearson, C.A.B., Russell, T.W., Tully, D.C., Washburne, A.D.*, et al.* (2021). Estimated transmissibility and impact of SARS-CoV-2 lineage B.1.1.7 in England. Science *372*.

Desmyter, J., Melnick, J.L., and Rawls, W.E. (1968). Defectiveness of interferon production and of rubella virus interference in a line of African green monkey kidney cells (Vero). J Virol *2*, 955-961.

Dhir, A., Dhir, S., Borowski, L.S., Jimenez, L., Teitell, M., Rotig, A., Crow, Y.J., Rice, G.I., Duffy, D., Tamby, C.*, et al.* (2018). Mitochondrial double-stranded RNA triggers antiviral signalling in humans. Nature *560*, 238-242.

Dicken, S.J., Murray, M.J., Thorne, L.G., Reuschl, A.K., Forrest, C., Ganeshalingham, M., Muir, L., Kalemera, M.D., Palor, M., McCoy, L.E.*, et al.* (2021). Characterisation of B.1.1.7 and Pangolin coronavirus spike provides insights on the evolutionary trajectory of SARS-CoV-2. bioRxiv.

Dinesh, D.C., Chalupska, D., Silhan, J., Koutna, E., Nencka, R., Veverka, V., and Boura, E. (2020). Structural basis of RNA recognition by the SARS-CoV-2 nucleocapsid phosphoprotein. PLoS Pathog *16*, e1009100.

Eymieux, S., Rouille, Y., Terrier, O., Seron, K., Blanchard, E., Rosa-Calatrava, M., Dubuisson, J., Belouzard, S., and Roingeard, P. (2021). Ultrastructural modifications induced by SARS-CoV-2 in Vero cells: a kinetic analysis of viral factory formation, viral particle morphogenesis and virion release. Cell Mol Life Sci *78*, 3565-3576.

Femino, A.M., Fay, F.S., Fogarty, K., and Singer, R.H. (1998). Visualization of single RNA transcripts in situ. Science *280*, 585-590.

Fiege, J.K., Thiede, J.M., Nanda, H.A., Matchett, W.E., Moore, P.J., Montanari, N.R., Thielen, B.K., Daniel, J., Stanley, E., Hunter, R.C.*, et al.* (2021). Single cell resolution of SARS-CoV-2 tropism, antiviral responses, and susceptibility to therapies in primary human airway epithelium. PLoS Pathog *17*, e1009292.

Fraser, D., and Kaern, M. (2009). A chance at survival: gene expression noise and phenotypic diversification strategies. Mol Microbiol *71*, 1333-1340.

Galloway, S.E., Paul, P., MacCannell, D.R., Johansson, M.A., Brooks, J.T., MacNeil, A., Slayton, R.B., Tong, S., Silk, B.J., Armstrong, G.L.*, et al.* (2021). Emergence of SARS-CoV-2 B.1.1.7 Lineage - United States, December 29, 2020-January 12, 2021. MMWR Morb Mortal Wkly Rep *70*, 95-99.

Garcia-Moreno, M., Noerenberg, M., Ni, S., Jarvelin, A.I., Gonzalez-Almela, E., Lenz, C.E., Bach-Pages, M., Cox, V., Avolio, R., Davis, T.*, et al.* (2019). System-wide Profiling of RNA-Binding Proteins Uncovers Key Regulators of Virus Infection. Mol Cell *74*, 196-211 e111.

Gaspar, I., Wippich, F., and Ephrussi, A. (2017). Enzymatic production of single-molecule FISH and RNA capture probes. RNA *23*, 1582-1591.

Guerini-Rocco, E., Taormina, S.V., Vacirca, D., Ranghiero, A., Rappa, A., Fumagalli, C., Maffini, F., Rampinelli, C., Galetta, D., Tagliabue, M.*, et al.* (2020). SARS-CoV-2 detection in formalin-fixed

paraffin-embedded tissue specimens from surgical resection of tongue squamous cell carcinoma. J Clin Pathol *73*, 754-757.

Healy, C.P., Adler, F.R., and Deans, T.L. (2020). Rolling Signal-based Ripley's K: A new algorithm to identify spatial patterns in histological specimens. bioRxiv, 2020.2005.2021.109314.

Hoffmann, M., Kleine-Weber, H., Schroeder, S., Kruger, N., Herrler, T., Erichsen, S., Schiergens, T.S., Herrler, G., Wu, N.H., Nitsche, A.*, et al.* (2020). SARS-CoV-2 Cell Entry Depends on ACE2 and TMPRSS2 and Is Blocked by a Clinically Proven Protease Inhibitor. Cell *181*, 271-280 e278.

Huang, K.-Y.A., Tan, T.K., Chen, T.-H., Huang, C.-G., Harvey, R., Hussain, S., Chen, C.-P., Harding, A., Gilbert-Jaramillo, J., Liu, X.*, et al.* (2020). Breadth and function of antibody response to acute SARS-CoV-2 infection in humans. bioRxiv, 2020.2008.2028.267526.

Iserman, C., Roden, C.A., Boerneke, M.A., Sealfon, R.S.G., McLaughlin, G.A., Jungreis, I., Fritch, E.J., Hou, Y.J., Ekena, J., Weidmann, C.A.*, et al.* (2020). Genomic RNA Elements Drive Phase Separation of the SARS-CoV-2 Nucleocapsid. Mol Cell *80*, 1078-1091 e1076.

Jiao, J., Duan, C., Xue, L., Liu, Y., Sun, W., and Xiang, Y. (2020). DNA nanoscaffold-based SARS-CoV-2 detection for COVID-19 diagnosis. Biosens Bioelectron *167*, 112479.

Kamel, W., Noerenberg, M., Cerikan, B., Chen, H., Jarvelin, A.I., Kammoun, M., Lee, J.Y., Shuai, N., Garcia-Moreno, M., Andrejeva, A.*, et al.* (2021). Global analysis of protein-RNA interactions in SARS-CoV-2-infected cells reveals key regulators of infection. Mol Cell.

Kidd, M., Richter, A., Best, A., Cumley, N., Mirza, J., Percival, B., Mayhew, M., Megram, O., Ashford, F., White, T.*, et al.* (2021). S-variant SARS-CoV-2 lineage B1.1.7 is associated with significantly higher viral loads in samples tested by ThermoFisher TaqPath RT-qPCR. J Infect Dis.

Kim, D., Lee, J.Y., Yang, J.S., Kim, J.W., Kim, V.N., and Chang, H. (2020). The Architecture of SARS-CoV-2 Transcriptome. Cell *181*, 914-921 e910.

Kimura, S., Matsumiya, T., Shiba, Y., Nakanishi, M., Hayakari, R., Kawaguchi, S., Yoshida, H., and Imaizumi, T. (2018). The Essential Role of Double-Stranded RNA-Dependent Antiviral Signaling in the Degradation of Nonself Single-Stranded RNA in Nonimmune Cells. J Immunol *201*, 1044-1052.

Kissler, S.M., Fauver, J.R., Mack, C., Tai, C.G., Breban, M.I., Watkins, A.E., Samant, R.M., Anderson, D.J., Ho, D.D., Grubaugh, N.D.*, et al.* (2021). Densely sampled viral trajectories suggest longer duration of acute infection with B.1.1.7 variant relative to non-B.1.1.7 SARS-CoV-2. medRxiv, 2021.2002.2016.21251535.

Klein, S., Cortese, M., Winter, S.L., Wachsmuth-Melm, M., Neufeldt, C.J., Cerikan, B., Stanifer, M.L., Boulant, S., Bartenschlager, R., and Chlanda, P. (2020). SARS-CoV-2 structure and replication characterized by in situ cryo-electron tomography. Nat Commun *11*, 5885.

Kusmartseva, I., Wu, W., Syed, F., Van Der Heide, V., Jorgensen, M., Joseph, P., Tang, X., Candelario-Jalil, E., Yang, C., Nick, H.*, et al.* (2020). Expression of SARS-CoV-2 Entry Factors in the Pancreas of Normal Organ Donors and Individuals with COVID-19. Cell Metab *32*, 1041-1051 e1046.

Langmead, B., and Salzberg, S.L. (2012). Fast gapped-read alignment with Bowtie 2. Nat Methods *9*, 357-359.

Laue, M., Kauter, A., Hoffmann, T., Moller, L., Michel, J., and Nitsche, A. (2021). Morphometry of SARS-CoV and SARS-CoV-2 particles in ultrathin plastic sections of infected Vero cell cultures. Sci Rep *11*, 3515.

Lean, F.Z.X., Lamers, M.M., Smith, S.P., Shipley, R., Schipper, D., Temperton, N., Haagmans, B.L., Banyard, A.C., Bewley, K.R., Carroll, M.W.*, et al.* (2020). Development of immunohistochemistry and

in situ hybridisation for the detection of SARS-CoV and SARS-CoV-2 in formalin-fixed paraffin-embedded specimens. Sci Rep *10*, 21894.

Li, Y., Renner, D.M., Comar, C.E., Whelan, J.N., Reyes, H.M., Cardenas-Diaz, F.L., Truitt, R., Tan, L.H., Dong, B., Alysandratos, K.D.*, et al.* (2021). SARS-CoV-2 induces double-stranded RNA-mediated innate immune responses in respiratory epithelial-derived cells and cardiomyocytes. Proc Natl Acad Sci U S A *118*.

Liu, J., Babka, A.M., Kearney, B.J., Radoshitzky, S.R., Kuhn, J.H., and Zeng, X. (2020). Molecular detection of SARS-CoV-2 in formalin-fixed, paraffin-embedded specimens. JCI Insight *5*.

Lythgoe, K.A., Hall, M., Ferretti, L., de Cesare, M., MacIntyre-Cockett, G., Trebes, A., Andersson, M., Otecko, N., Wise, E.L., Moore, N.*, et al.* (2021). SARS-CoV-2 within-host diversity and transmission. Science *372*.

Maneewongvatana, S., and Mount, D. (1999). Analysis of approximate nearest neighbor searching with clustered point sets. Paper presented at: Data Structures, Near Neighbor Searches, and Methodology.

Mueller, F., Senecal, A., Tantale, K., Marie-Nelly, H., Ly, N., Collin, O., Basyuk, E., Bertrand, E., Darzacq, X., and Zimmer, C. (2013). FISH-quant: automatic counting of transcripts in 3D FISH images. Nat Methods *10*, 277-278.

Mullen, P.J., Garcia, G., Jr., Purkayastha, A., Matulionis, N., Schmid, E.W., Momcilovic, M., Sen, C., Langerman, J., Ramaiah, A., Shackelford, D.B.*, et al.* (2021). SARS-CoV-2 infection rewires host cell metabolism and is potentially susceptible to mTORC1 inhibition. Nat Commun *12*, 1876.

Planas, D., Bruel, T., Grzelak, L., Guivel-Benhassine, F., Staropoli, I., Porrot, F., Planchais, C., Buchrieser, J., Rajah, M.M., Bishop, E.*, et al.* (2021). Sensitivity of infectious SARS-CoV-2 B.1.1.7 and B.1.351 variants to neutralizing antibodies. Nat Med *27*, 917-924.

Raj, A., van den Bogaard, P., Rifkin, S.A., van Oudenaarden, A., and Tyagi, S. (2008). Imaging individual mRNA molecules using multiple singly labeled probes. Nat Methods *5*, 877-879.

Raj, A., and van Oudenaarden, A. (2009). Single-molecule approaches to stochastic gene expression. Annu Rev Biophys *38*, 255-270.

Ramanan, V., Trehan, K., Ong, M.L., Luna, J.M., Hoffmann, H.H., Espiritu, C., Sheahan, T.P., Chandrasekar, H., Schwartz, R.E., Christine, K.S.*, et al.* (2016). Viral genome imaging of hepatitis C virus to probe heterogeneous viral infection and responses to antiviral therapies. Virology *494*, 236-247.

Ravindra, N.G., Alfajaro, M.M., Gasque, V., Huston, N.C., Wan, H., Szigeti-Buck, K., Yasumoto, Y., Greaney, A.M., Habet, V., Chow, R.D.*, et al.* (2021). Single-cell longitudinal analysis of SARS-CoV-2 infection in human airway epithelium identifies target cells, alterations in gene expression, and cell state changes. PLoS Biol *19*, e3001143.

Rees-Spear, C., Muir, L., Griffith, S.A., Heaney, J., Aldon, Y., Snitselaar, J.L., Thomas, P., Graham, C., Seow, J., Lee, N.*, et al.* (2021). The effect of spike mutations on SARS-CoV-2 neutralization. Cell Rep *34*, 108890.

Rensen, E., Pietropaoli, S., Mueller, F., Weber, C., Souquere, S., Isnard, P., Rabant, M., Gibier, J.-B., Simon-Loriere, E., Rameix-Welti, M.-A.*, et al.* (2021). Sensitive visualization of SARS-CoV-2 RNA with CoronaFISH. bioRxiv, 2021.2002.2004.429604.

Ripley, B.D. (1979). Tests of `Randomness' for Spatial Point Patterns. Journal of the Royal Statistical Society Series B (Methodological) *41*, 368-374.

Salguero, F.J., White, A.D., Slack, G.S., Fotheringham, S.A., Bewley, K.R., Gooch, K.E., Longet, S., Humphries, H.E., Watson, R.J., Hunter, L.*, et al.* (2021). Comparison of rhesus and cynomolgus macaques as an infection model for COVID-19. Nat Commun *12*, 1260.

Schoggins, J.W., and Rice, C.M. (2011). Interferon-stimulated genes and their antiviral effector functions. Curr Opin Virol *1*, 519-525.

Sethna, P.B., Hofmann, M.A., and Brian, D.A. (1991). Minus-strand copies of replicating coronavirus mRNAs contain antileaders. J Virol *65*, 320-325.

Shulla, A., and Randall, G. (2015). Spatiotemporal analysis of hepatitis C virus infection. PLoS Pathog *11*, e1004758.

Simmonds, P., Williams, S., and Harvala, H. (2021). Understanding the outcomes of COVID-19 - does the current model of an acute respiratory infection really fit? J Gen Virol *102*.

Singer, Z.S., Ambrose, P.M., Danino, T., and Rice, C.M. (2021). Quantitative measurements of early alphaviral replication dynamics in single cells reveals the basis for superinfection exclusion. Cell Syst *12*, 210-219 e213.

Sola, I., Almazan, F., Zuniga, S., and Enjuanes, L. (2015). Continuous and Discontinuous RNA Synthesis in Coronaviruses. Annu Rev Virol *2*, 265-288.

Stringer, C., Wang, T., Michaelos, M., and Pachitariu, M. (2021). Cellpose: a generalist algorithm for cellular segmentation. Nat Methods *18*, 100-106.

Targett-Adams, P., Boulant, S., and McLauchlan, J. (2008). Visualization of double-stranded RNA in cells supporting hepatitis C virus RNA replication. J Virol *82*, 2182-2195.

Tegally, H., Wilkinson, E., Giovanetti, M., Iranzadeh, A., Fonseca, V., Giandhari, J., Doolabh, D., Pillay, S., San, E.J., Msomi, N.*, et al.* (2020). Emergence and rapid spread of a new severe acute respiratory syndrome-related coronavirus 2 (SARS-CoV-2) lineage with multiple spike mutations in South Africa. medRxiv, 2020.2012.2021.20248640.

Thorne, L.G., Bouhaddou, M., Reuschl, A.-K., Zuliani-Alvarez, L., Polacco, B., Pelin, A., Batra, J., Whelan, M.V.X., Ummadi, M., Rojc, A.*, et al.* (2021a). Evolution of enhanced innate immune evasion by the SARS-CoV-2 B.1.1.7 UK variant. bioRxiv, 2021.2006.2006.446826.

Thorne, L.G., Reuschl, A.K., Zuliani-Alvarez, L., Whelan, M.V.X., Turner, J., Noursadeghi, M., Jolly, C., and Towers, G.J. (2021b). SARS-CoV-2 sensing by RIG-I and MDA5 links epithelial infection to macrophage inflammation. EMBO J, e107826.

Titlow, J.S., Yang, L., Parton, R.M., Palanca, A., and Davis, I. (2018). Super-Resolution Single Molecule FISH at the Drosophila Neuromuscular Junction. Methods Mol Biol *1649*, 163-175.

V'Kovski, P., Kratzel, A., Steiner, S., Stalder, H., and Thiel, V. (2021). Coronavirus biology and replication: implications for SARS-CoV-2. Nat Rev Microbiol *19*, 155-170.

Volz, E., Mishra, S., Chand, M., Barrett, J.C., Johnson, R., Geidelberg, L., Hinsley, W.R., Laydon, D.J., Dabrera, G., O'Toole, A.*, et al.* (2021). Assessing transmissibility of SARS-CoV-2 lineage B.1.1.7 in England. Nature *593*, 266-269.

Wan, Y., Shang, J., Graham, R., Baric, R.S., and Li, F. (2020). Receptor Recognition by the Novel Coronavirus from Wuhan: an Analysis Based on Decade-Long Structural Studies of SARS Coronavirus. J Virol *94*.

Washington, N.L., Gangavarapu, K., Zeller, M., Bolze, A., Cirulli, E.T., Schiabor Barrett, K.M., Larsen, B.B., Anderson, C., White, S., Cassens, T.*, et al.* (2021). Emergence and rapid transmission of SARS-CoV-2 B.1.1.7 in the United States. Cell *184*, 2587-2594 e2587.

Weber, F., Wagner, V., Rasmussen, S.B., Hartmann, R., and Paludan, S.R. (2006). Double-stranded RNA is produced by positive-strand RNA viruses and DNA viruses but not in detectable amounts by negative-strand RNA viruses. J Virol *80*, 5059-5064.

Wilcox, A.H., Delwart, E., and Diaz-Munoz, S.L. (2019). Next-generation sequencing of dsRNA is greatly improved by treatment with the inexpensive denaturing reagent DMSO. Microb Genom *5*.

Wing, P.A.C., Keeley, T.P., Zhuang, X., Lee, J.Y., Prange-Barczynska, M., Tsukuda, S., Morgan, S.B., Harding, A.C., Argles, I.L.A., Kurlekar, S.*, et al.* (2021). Hypoxic and pharmacological activation of HIF inhibits SARS-CoV-2 infection of lung epithelial cells. Cell Rep *35*, 109020.

Wolff, G., Melia, C.E., Snijder, E.J., and Barcena, M. (2020). Double-Membrane Vesicles as Platforms for Viral Replication. Trends Microbiol *28*, 1022-1033.

Yang, L., Titlow, J., Ennis, D., Smith, C., Mitchell, J., Young, F.L., Waddell, S., Ish-Horowicz, D., and Davis, I. (2017). Single molecule fluorescence in situ hybridisation for quantitating post-transcriptional regulation in Drosophila brains. Methods *126*, 166-176.

Yin, X., Riva, L., Pu, Y., Martin-Sancho, L., Kanamune, J., Yamamoto, Y., Sakai, K., Gotoh, S., Miorin, L., De Jesus, P.D.*, et al.* (2021). MDA5 Governs the Innate Immune Response to SARS-CoV-2 in Lung Epithelial Cells. Cell Rep *34*, 108628.

Zhao, M., Yu, Y., Sun, L.M., Xing, J.Q., Li, T., Zhu, Y., Wang, M., Yu, Y., Xue, W., Xia, T.*, et al.* (2021). GCG inhibits SARS-CoV-2 replication by disrupting the liquid phase condensation of its nucleocapsid protein. Nat Commun *12*, 2114.

Figure 1

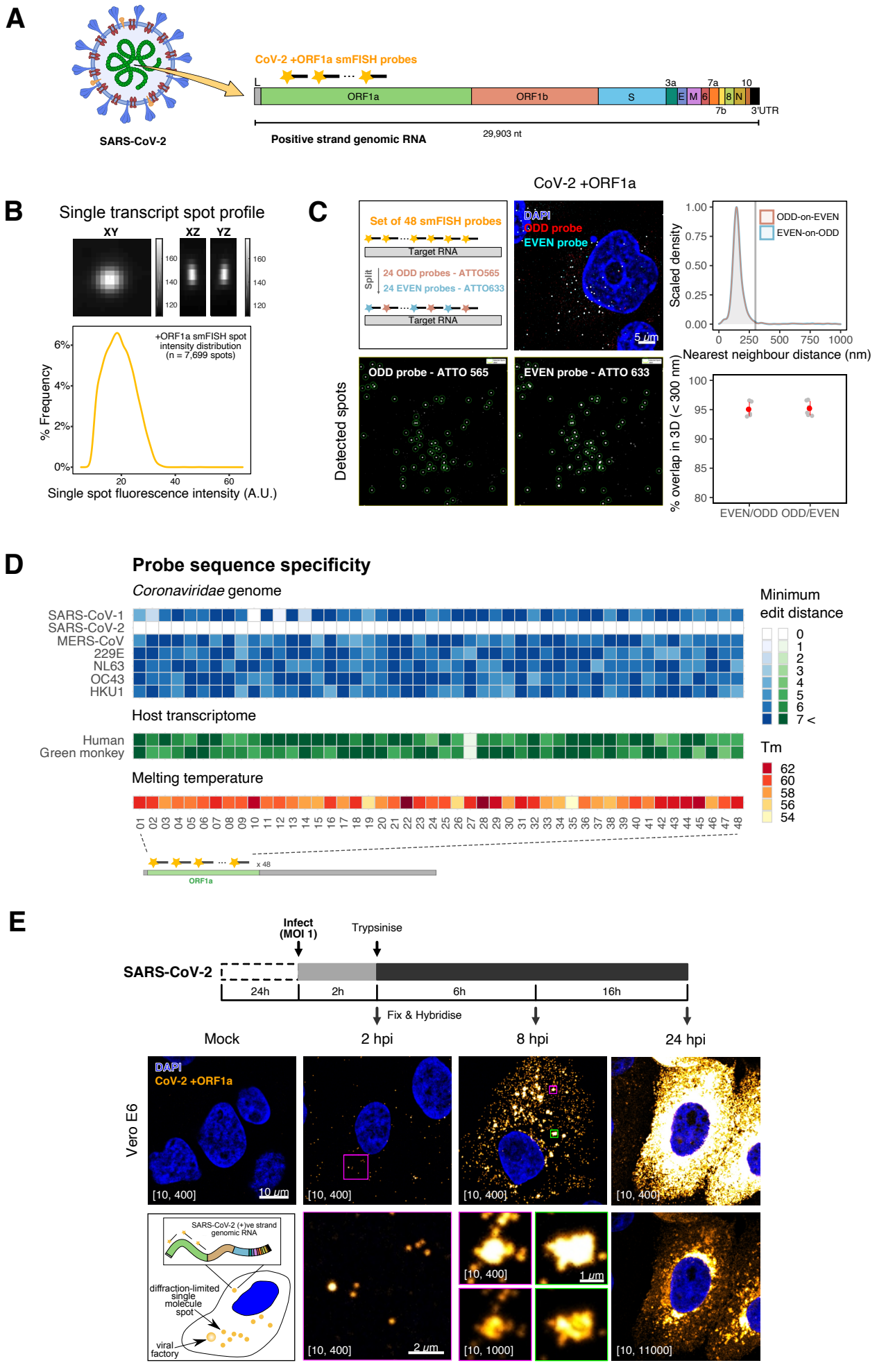
A
SARS-CoV-2
CoV-2 +ORF1a smFISH probes
L
ORF1a
ORF1b
S
3a
E
M
6
7a
7b
8
N
10
3'UTR
Positive strand genomic RNA
29,903 nt
B
Single transcript spot profile
XY
XZ
YZ
160
140
120
+ORF1a smFISH spot intensity distribution (n = 7,699 spots)
% Frequency
6%
4%
2%
0%
20
40
60
Single spot fluorescence intensity (A.U.)
C
CoV-2 +ORF1a
Set of 48 smFISH probes
Target RNA
Split
24 ODD probes - ATTO565
24 EVEN probes - ATTO633
Target RNA
DAPI
ODD probe
EVEN probe
5 µm
Scaled density
1.00
0.75
0.50
0.25
0.00
ODD-on-EVEN
EVEN-on-ODD
0
250
500
750
1000
Nearest neighbour distance (nm)
Detected spots
ODD probe - ATTO 565
EVEN probe - ATTO 633
% overlap in 3D (< 300 nm)
100
95
90
85
80
EVEN/ODD
ODD/EVEN
D
Probe sequence specificity
Coronaviridae genome
SARS-CoV-1
SARS-CoV-2
MERS-CoV
229E
NL63
OC43
HKU1
Minimum edit distance
0
1
2
3
4
5
6
7 <
Host transcriptome
Human
Green monkey
Melting temperature
Tm
62
60
58
56
54
01 02 03 04 05 06 07 08 09 10 11 12 13 14 15 16 17 18 19 20 21 22 23 24 25 26 27 28 29 30 31 32 33 34 35 36 37 38 39 40 41 42 43 44 45 46 47 48
x 48
ORF1a
E
Infect (MOI 1)
Trypsinise
SARS-CoV-2
24h
2h
6h
16h
Fix & Hybridise
Mock
2 hpi
8 hpi
24 hpi
Vero E6
DAPI
CoV-2 +ORF1a
[10, 400]
10 µm
SARS-CoV-2 (+)ve strand genomic RNA
diffraction-limited single molecule spot
viral factory
2 µm
1 µm
[10, 1000]
[10, 11000]

Figure S1

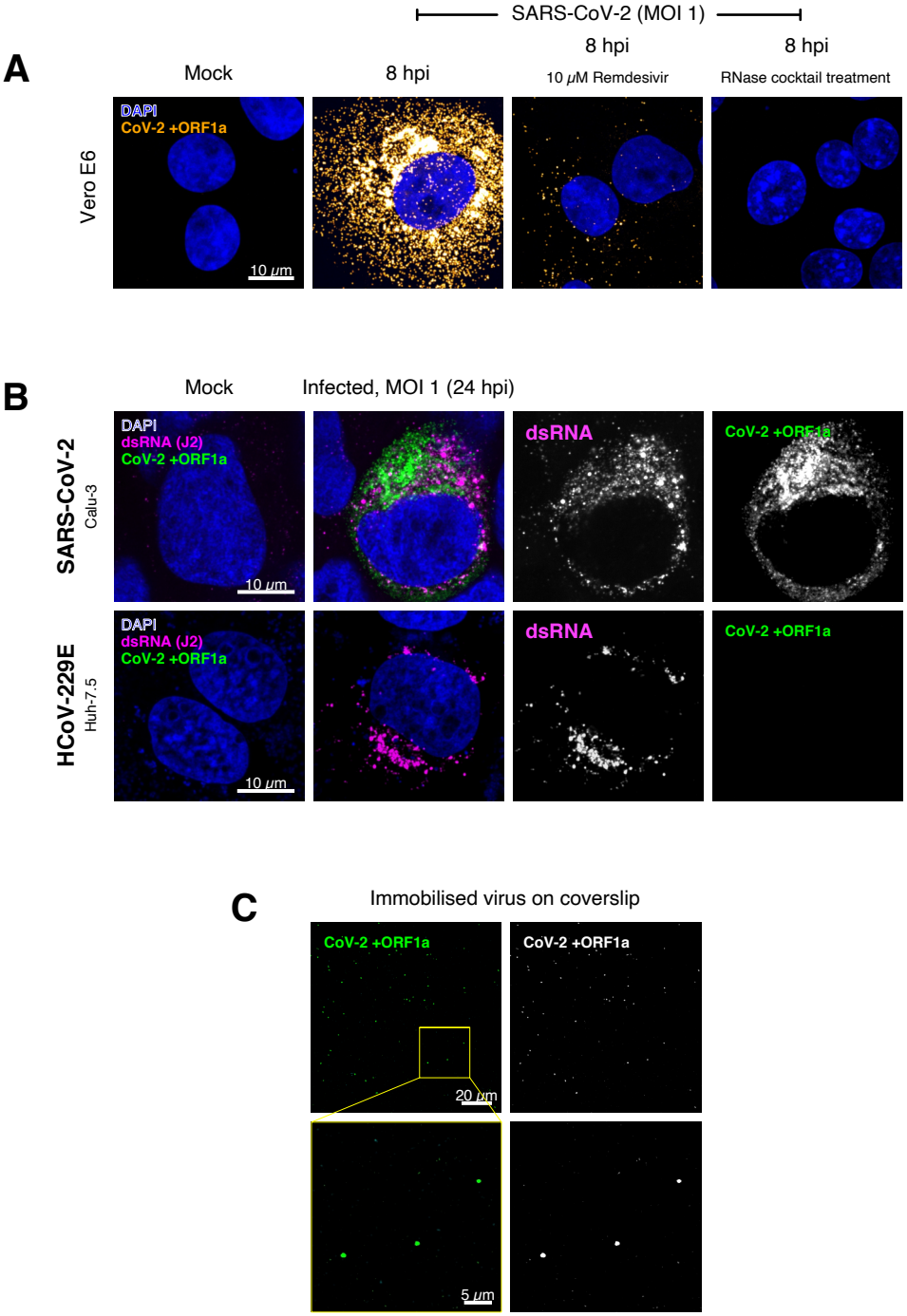
A
SARS-CoV-2 (MOI 1)
Mock
8 hpi
8 hpi
10 μM Remdesivir
8 hpi
RNase cocktail treatment
Vero E6
DAPI
CoV-2 +ORF1a
10 μm
B
Mock
Infected, MOI 1 (24 hpi)
SARS-CoV-2
Calu-3
HCoV-229E
Huh-7.5
DAPI
dsRNA (J2)
CoV-2 +ORF1a
dsRNA
CoV-2 +ORF1a
10 μm
C
Immobilised virus on coverslip
CoV-2 +ORF1a
CoV-2 +ORF1a
20 μm
5 μm

Figure 2

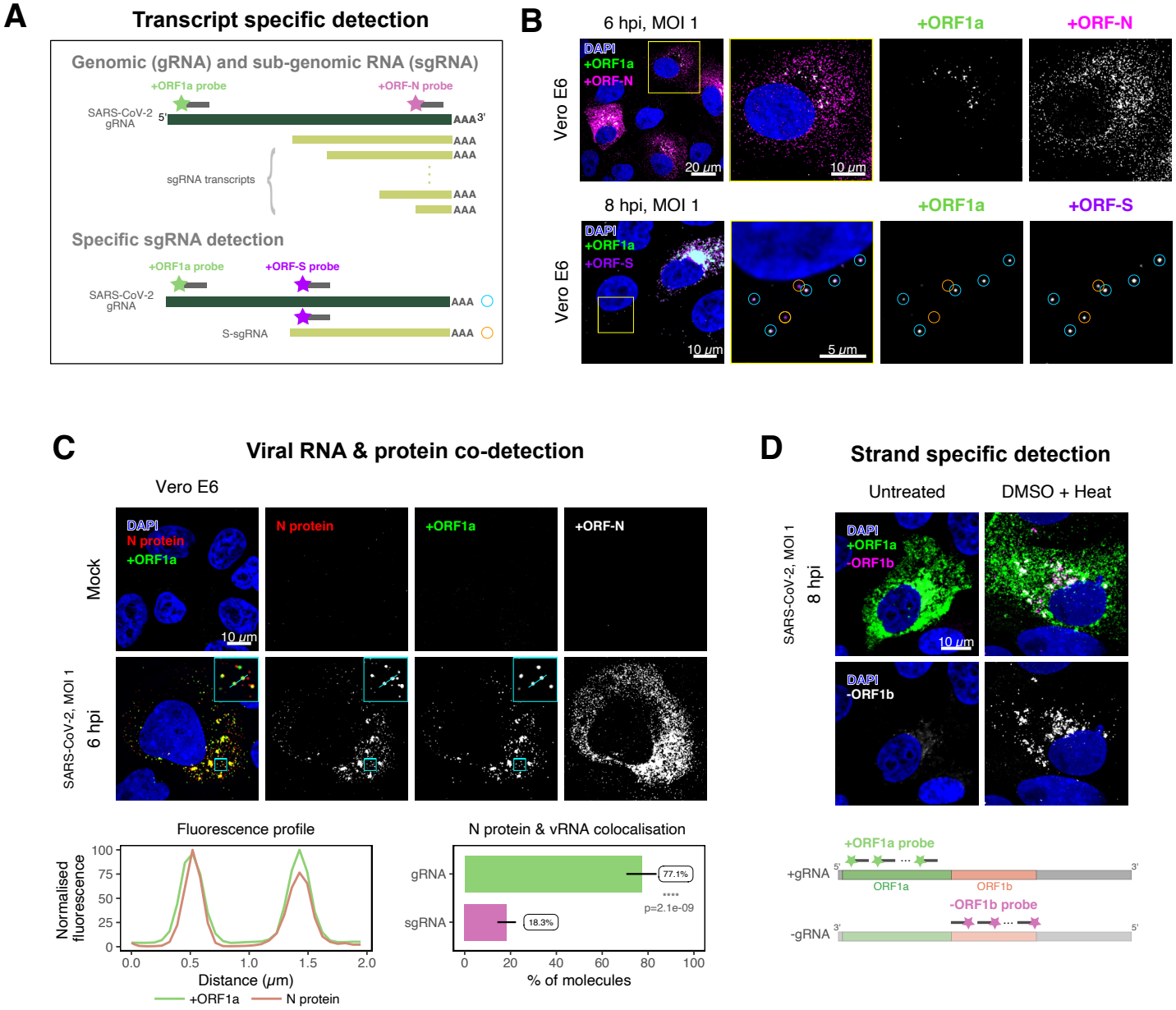
A
Transcript specific detection
Genomic (gRNA) and sub-genomic RNA (sgRNA)
+ORF1a probe
+ORF-N probe
SARS-CoV-2 gRNA
5'
AAA 3'
AAA
sgRNA transcripts
Specific sgRNA detection
+ORF1a probe
+ORF-S probe
S-sgRNA
B
6 hpi, MOI 1
+ORF1a
+ORF-N
Vero E6
DAPI
20 μm
10 μm
8 hpi, MOI 1
+ORF-S
5 μm
C
Viral RNA & protein co-detection
Vero E6
Mock
SARS-CoV-2, MOI 1
6 hpi
N protein
Fluorescence profile
Normalised fluorescence
Distance (μm)
N protein & vRNA colocalisation
gRNA
sgRNA
77.1%
18.3%
p=2.1e-09
% of molecules
D
Strand specific detection
Untreated
DMSO + Heat
SARS-CoV-2, MOI 1
8 hpi
-ORF1b
+ORF1a probe
+gRNA
ORF1a
ORF1b
-ORF1b probe
-gRNA
E
SARS-CoV-2, MOI 1
Mock
2 hpi
6 hpi
dsRNA
F
% dsRNA (J2) positive
% smFISH positive
% cells above 95th percentile Mock fluorescence
% fluorescence positive cells
p=6.9e-3
n.s.
p=0.675
p=3.3e-6
p=0.55
J2 intensity
smFISH gRNA count
Normalised fluorescence density
RNA count + 1 (log10)
p=1.1e-4
p=0.04

Figure S2

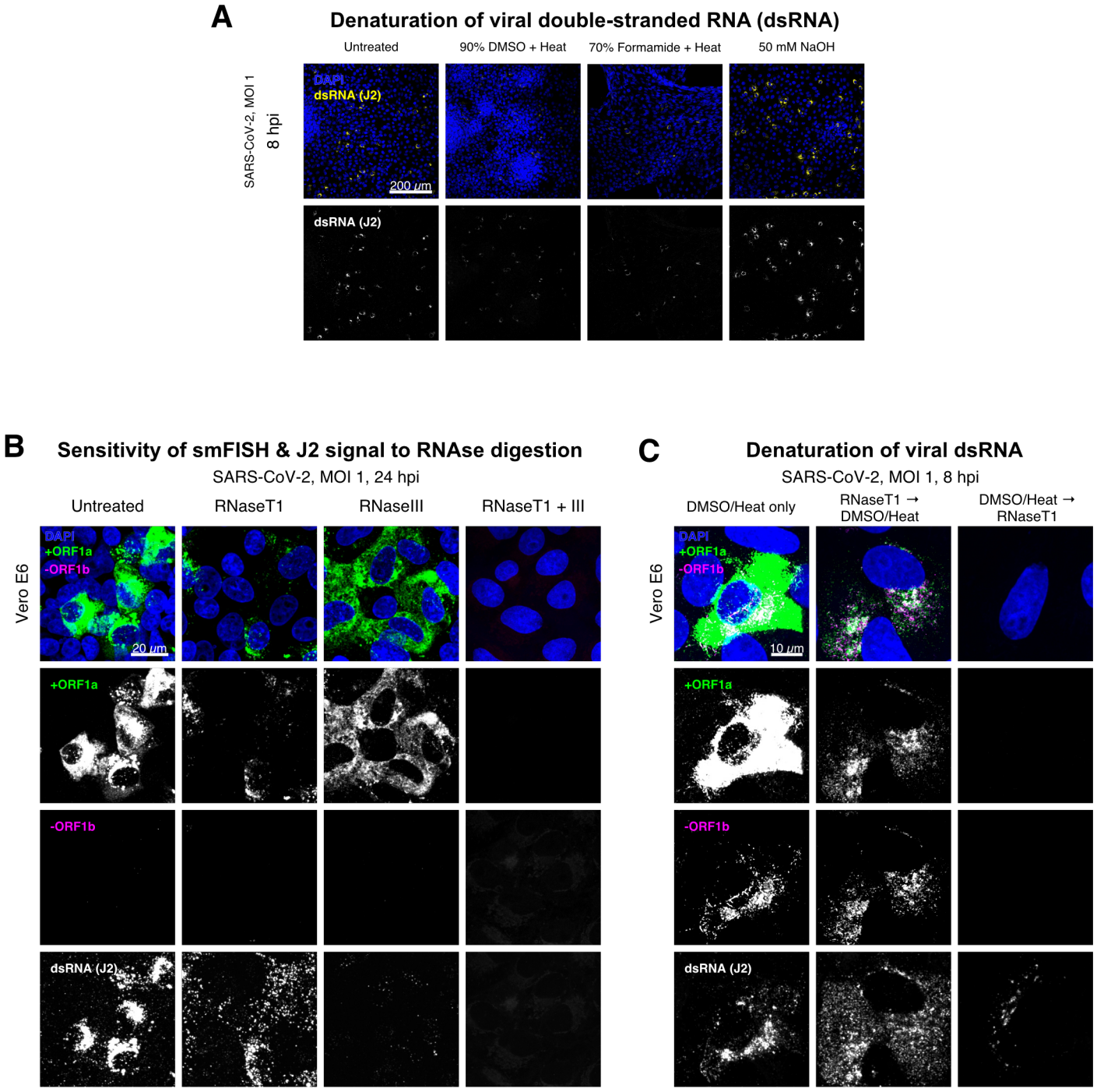
A
Denaturation of viral double-stranded RNA (dsRNA)
Untreated
90% DMSO + Heat
70% Formamide + Heat
50 mM NaOH
SARS-CoV-2, MOI 1
8 hpi
DAPI
dsRNA (J2)
200 μm
dsRNA (J2)
B
Sensitivity of smFISH & J2 signal to RNAse digestion
SARS-CoV-2, MOI 1, 24 hpi
Untreated
RNaseT1
RNaseIII
RNaseT1 + III
Vero E6
DAPI
+ORF1a
-ORF1b
20 μm
+ORF1a
-ORF1b
dsRNA (J2)
C
Denaturation of viral dsRNA
SARS-CoV-2, MOI 1, 8 hpi
DMSO/Heat only
RNaseT1 → DMSO/Heat
DMSO/Heat → RNaseT1
Vero E6
DAPI
+ORF1a
-ORF1b
10 μm
+ORF1a
-ORF1b
dsRNA (J2)

Figure 3

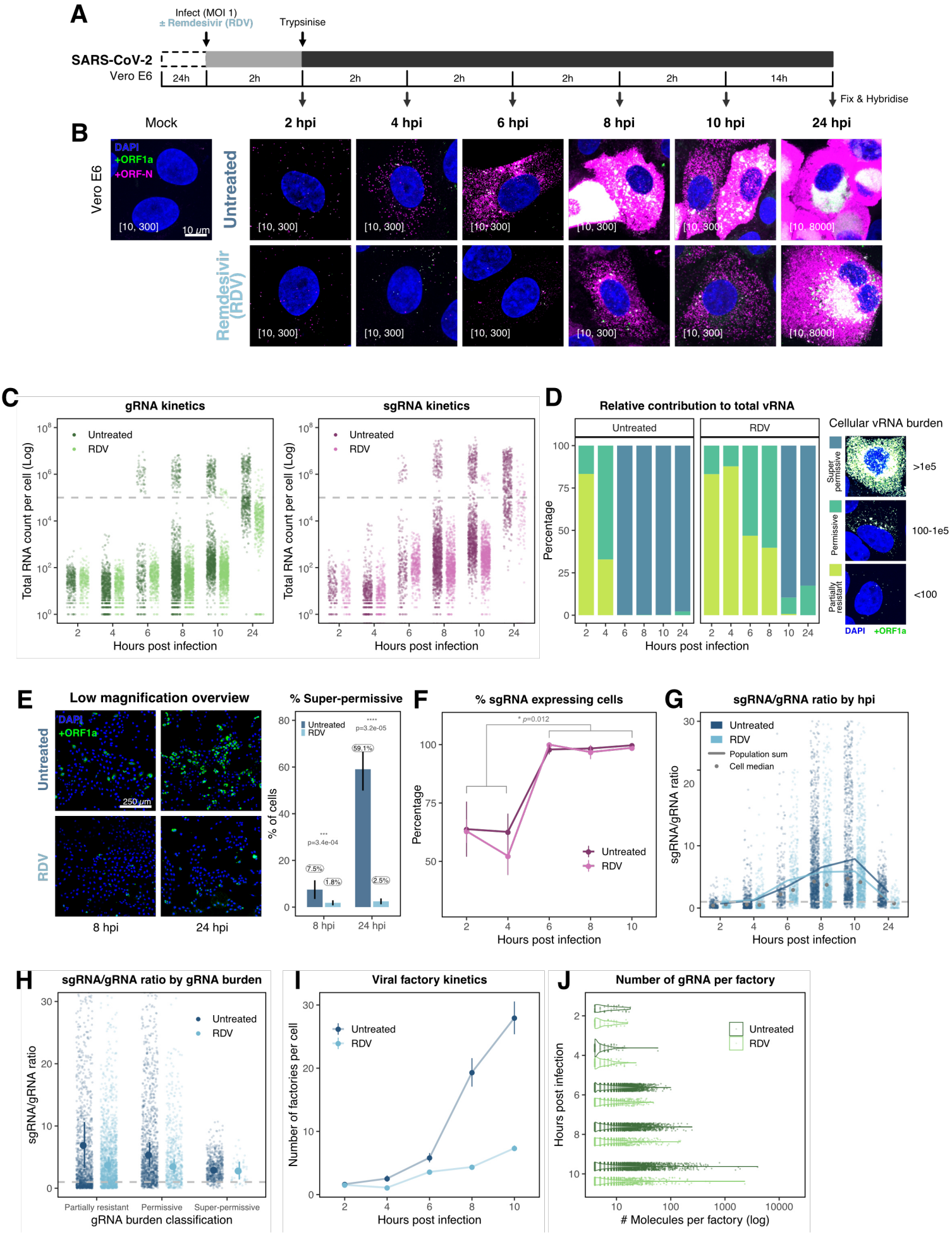
A
Infect (MOI 1)
± Remdesivir (RDV)
Trypsinise
SARS-CoV-2
Vero E6
24h
2h
2h
2h
2h
2h
14h
Fix & Hybridise
B
Mock
2 hpi
4 hpi
6 hpi
8 hpi
10 hpi
24 hpi
Vero E6
DAPI
+ORF1a
+ORF-N
[10, 300]
10 µm
Untreated
Remdesivir (RDV)
[10, 8000]
C
gRNA kinetics
sgRNA kinetics
Untreated
RDV
Total RNA count per cell (Log)
Hours post infection
D
Relative contribution to total vRNA
Untreated
RDV
Percentage
Hours post infection
Cellular vRNA burden
Super permissive
Permissive
Partially resistant
>1e5
100-1e5
<100
DAPI
+ORF1a
E
Low magnification overview
Untreated
RDV
250 µm
8 hpi
24 hpi
% Super-permissive
% of cells
p=3.2e-05
p=3.4e-04
59.1%
7.5%
1.8%
2.5%
F
% sgRNA expressing cells
* p=0.012
Percentage
Hours post infection
G
sgRNA/gRNA ratio by hpi
Population sum
Cell median
sgRNA/gRNA ratio
Hours post infection
H
sgRNA/gRNA ratio by gRNA burden
sgRNA/gRNA ratio
Partially resistant
Permissive
Super-permissive
gRNA burden classification
I
Viral factory kinetics
Number of factories per cell
Hours post infection
J
Number of gRNA per factory
Hours post infection
Molecules per factory (log)

Figure S3

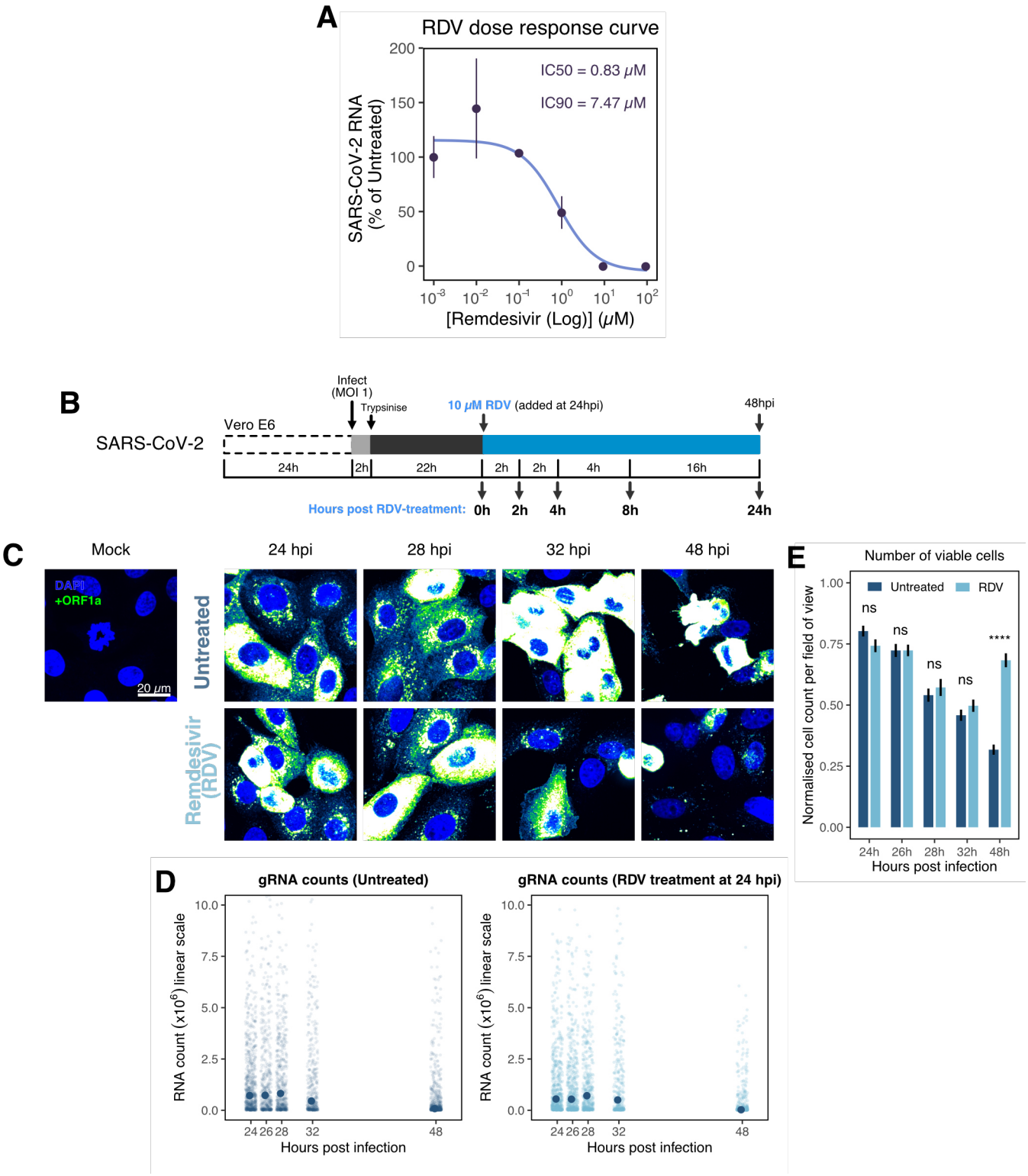
A
RDV dose response curve
IC50 = 0.83 μM
IC90 = 7.47 μM
SARS-CoV-2 RNA (% of Untreated)
[Remdesivir (Log)] (μM)
B
SARS-CoV-2
Vero E6
Infect (MOI 1)
Trypsinise
10 μM RDV (added at 24hpi)
48hpi
24h
2h
22h
2h
2h
4h
16h
Hours post RDV-treatment:
0h
2h
4h
8h
24h
C
Mock
24 hpi
28 hpi
32 hpi
48 hpi
DAPI
+ORF1a
20 μm
Untreated
Remdesivir (RDV)
D
gRNA counts (Untreated)
gRNA counts (RDV treatment at 24 hpi)
RNA count (x10^6) linear scale
Hours post infection
E
Number of viable cells
Untreated
RDV
Normalised cell count per field of view
ns
****
Hours post infection

Figure 4

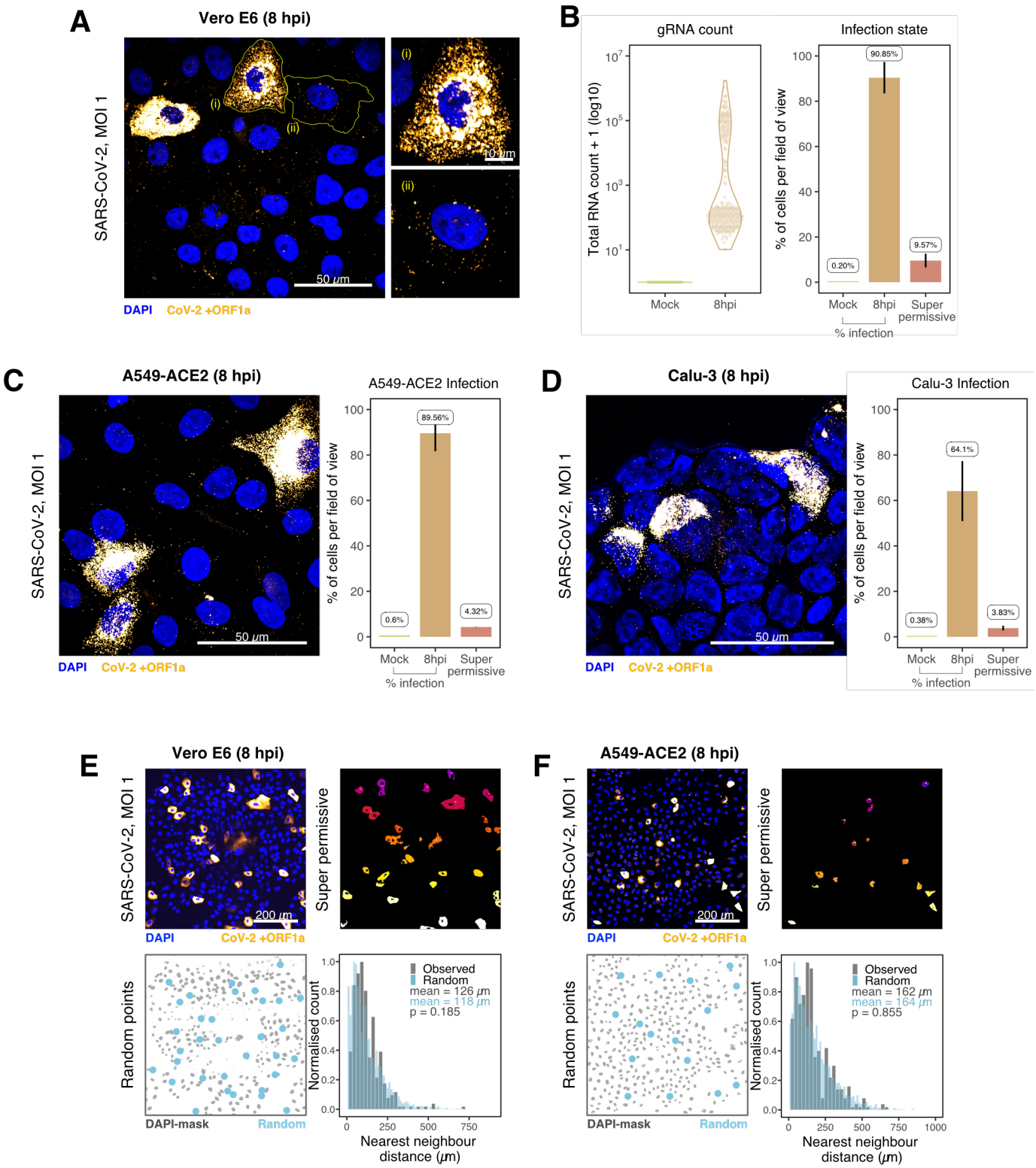
A
Vero E6 (8 hpi)
SARS-CoV-2, MOI 1
(i)
(ii)
50 μm
10 μm
DAPI
CoV-2 +ORF1a
B
gRNA count
Infection state
Total RNA count + 1 (log10)
% of cells per field of view
90.85%
9.57%
0.20%
Mock
8hpi
Super permissive
% infection
C
A549-ACE2 (8 hpi)
A549-ACE2 Infection
89.56%
0.6%
4.32%
D
Calu-3 (8 hpi)
Calu-3 Infection
64.1%
0.38%
3.83%
E
Vero E6 (8 hpi)
Super permissive
200 μm
Random points
DAPI-mask
Random
Normalised count
Observed
Random
mean = 126 μm
mean = 118 μm
p = 0.185
Nearest neighbour distance (μm)
F
A549-ACE2 (8 hpi)
mean = 162 μm
mean = 164 μm
p = 0.855

Figure S4

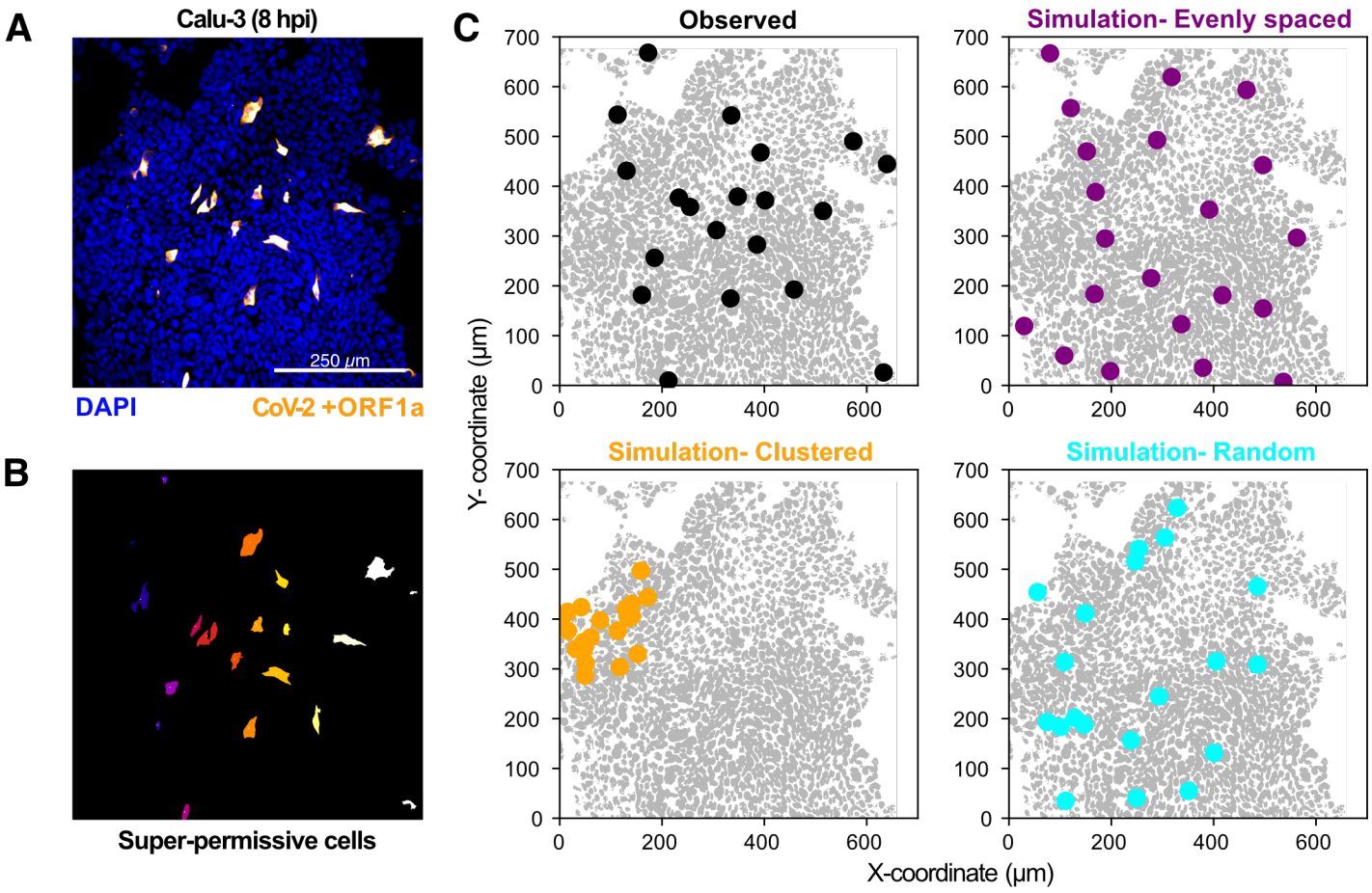
A
Calu-3 (8 hpi)
250 μm
DAPI
CoV-2 +ORF1a
B
Super-permissive cells
C
Observed
Simulation- Evenly spaced
Simulation- Clustered
Simulation- Random
Y- coordinate (μm)
X-coordinate (μm)
0
100
200
300
400
500
600
700

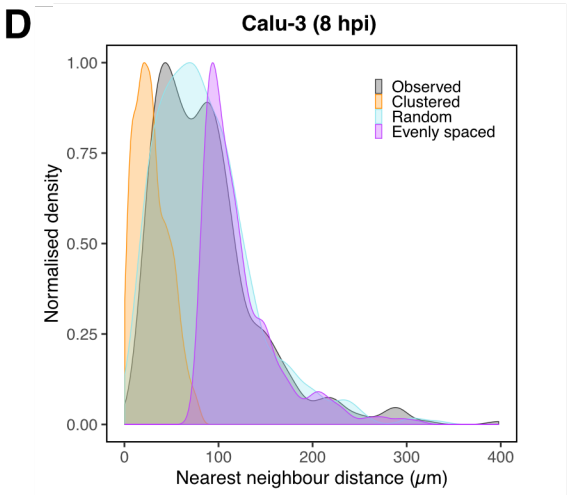
D
Calu-3 (8 hpi)
Observed
Clustered
Random
Evenly spaced
Normalised density
Nearest neighbour distance (μm)
0.00
0.25
0.50
0.75
1.00
0
100
200
300
400

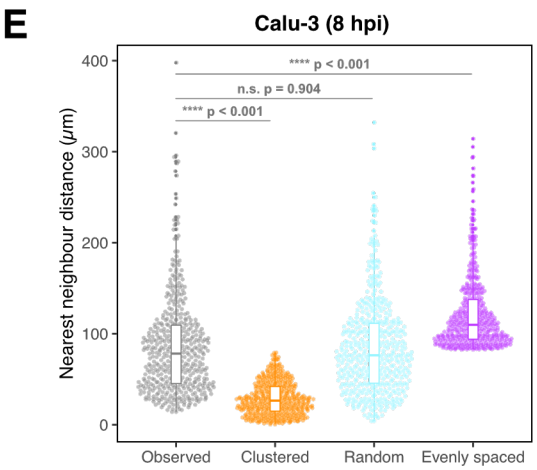
E
Calu-3 (8 hpi)
**** p < 0.001
n.s. p = 0.904
**** p < 0.001
Nearest neighbour distance (μm)
0
100
200
300
400
Observed
Clustered
Random
Evenly spaced

Figure 5

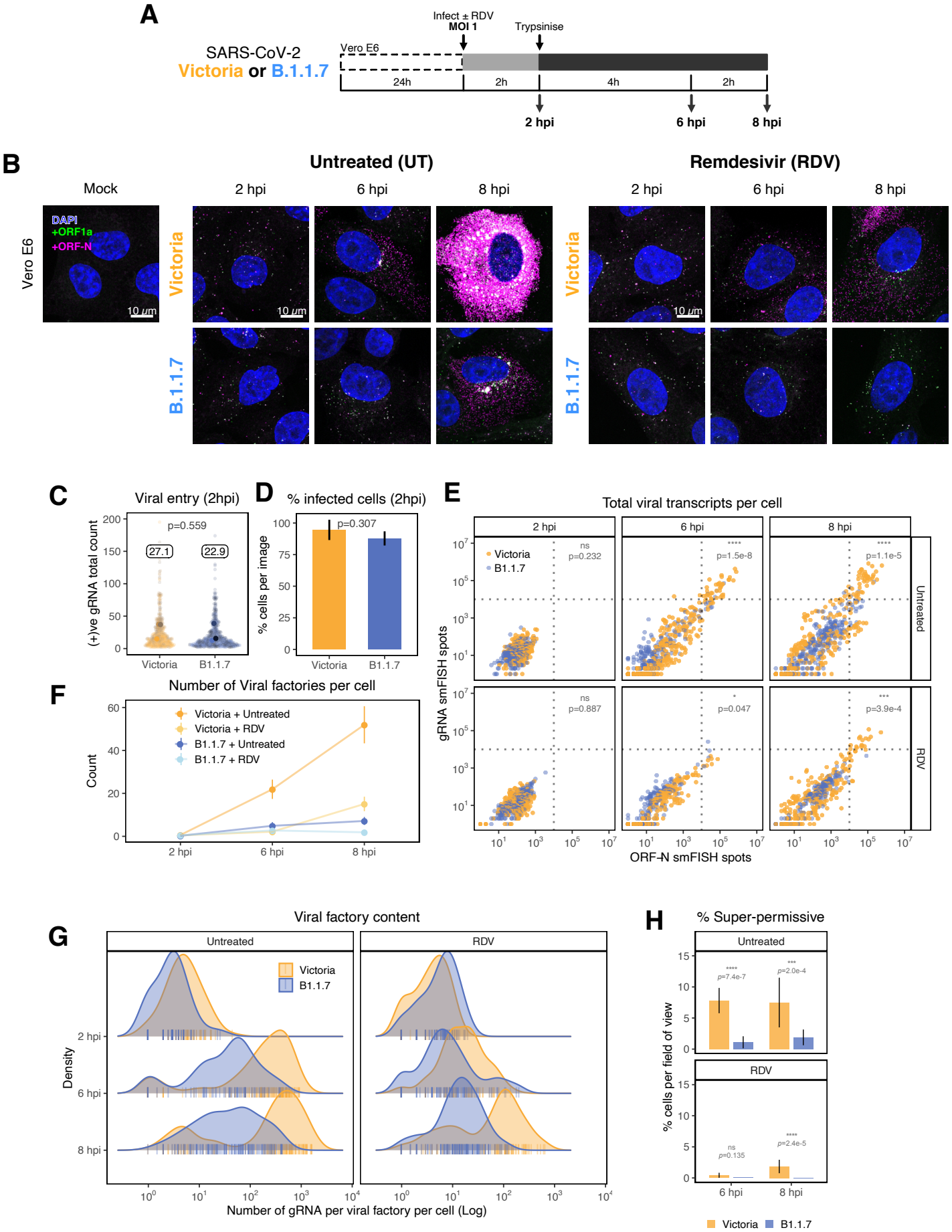
A
SARS-CoV-2
Victoria or B.1.1.7
Vero E6
Infect ± RDV
MOI 1
Trypsinise
24h
2h
4h
2h
2 hpi
6 hpi
8 hpi
B
Untreated (UT)
Remdesivir (RDV)
Mock
2 hpi
6 hpi
8 hpi
Vero E6
DAPI
+ORF1a
+ORF-N
10 µm
Victoria
B.1.1.7
C
Viral entry (2hpi)
(+)ve gRNA total count
p=0.559
27.1
22.9
Victoria
B1.1.7
D
% infected cells (2hpi)
% cells per image
p=0.307
E
Total viral transcripts per cell
Victoria
B1.1.7
ns
p=0.232
****
p=1.5e-8
p=1.1e-5
Untreated
ns
p=0.887
*
p=0.047
***
p=3.9e-4
RDV
gRNA smFISH spots
ORF-N smFISH spots
F
Number of Viral factories per cell
Count
Victoria + Untreated
Victoria + RDV
B1.1.7 + Untreated
B1.1.7 + RDV
G
Viral factory content
Density
Number of gRNA per viral factory per cell (Log)
H
% Super-permissive
% cells per field of view
****
p=7.4e-7
***
p=2.0e-4
ns
p=0.135
****
p=2.4e-5

Figure S5

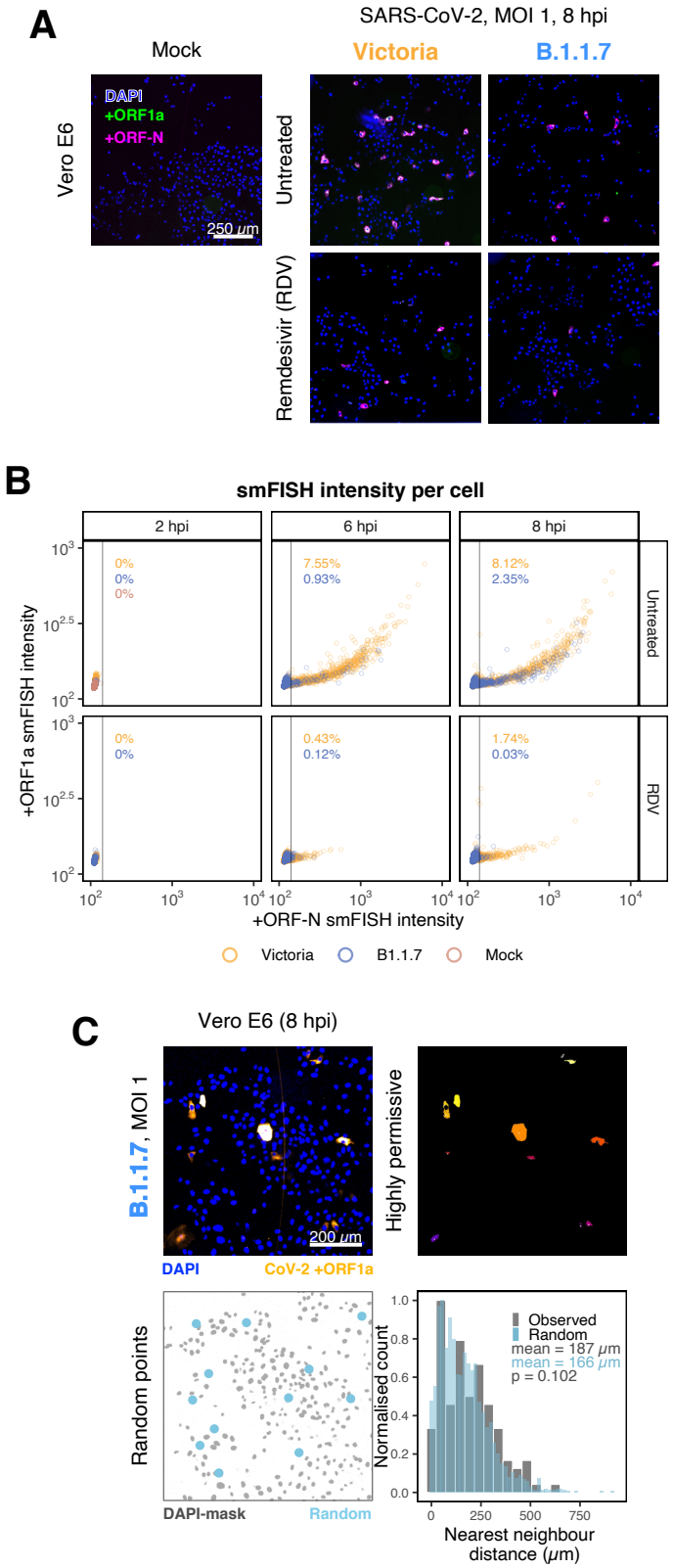
A
SARS-CoV-2, MOI 1, 8 hpi
Mock
Victoria
B.1.1.7
Vero E6
DAPI
+ORF1a
+ORF-N
250 µm
Untreated
Remdesivir (RDV)
B
smFISH intensity per cell
2 hpi
6 hpi
8 hpi
0%
0%
0%
7.55%
0.93%
8.12%
2.35%
0%
0%
0.43%
0.12%
1.74%
0.03%
Untreated
RDV
+ORF1a smFISH intensity
+ORF-N smFISH intensity
Victoria
B1.1.7
Mock
C
Vero E6 (8 hpi)
B.1.1.7, MOI 1
Highly permissive
200 µm
DAPI
CoV-2 +ORF1a
Random points
DAPI-mask
Random
Normalised count
Observed
Random
mean = 187 µm
mean = 166 µm
p = 0.102
Nearest neighbour distance (µm)

Figure 6

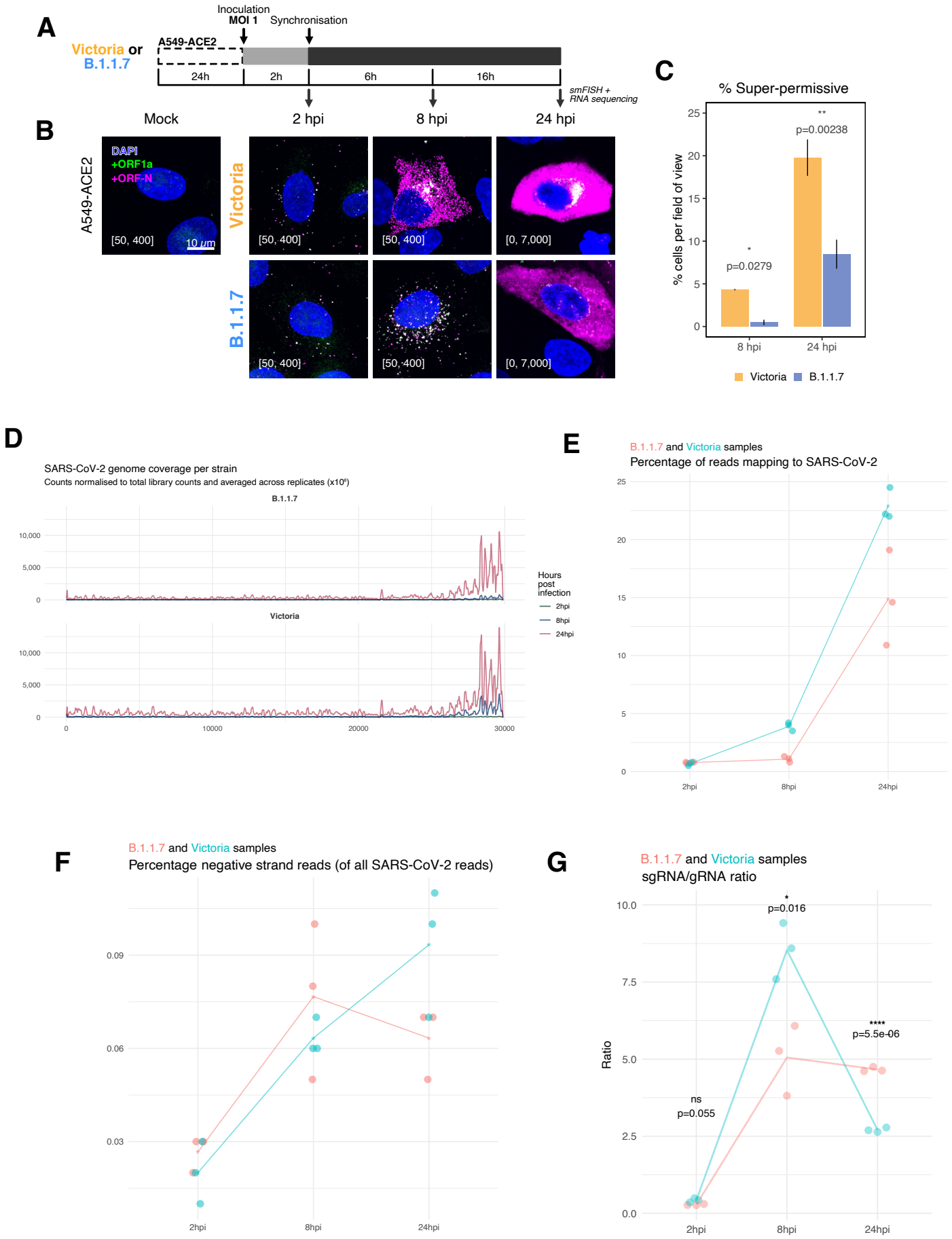
A
Inoculation
MOI 1
Synchronisation
Victoria or
B.1.1.7
A549-ACE2
24h
2h
6h
16h
smFISH +
RNA sequencing
B
Mock
2 hpi
8 hpi
24 hpi
A549-ACE2
DAPI
+ORF1a
+ORF-N
[50, 400]
10 µm
Victoria
B.1.1.7
[50, 400]
[50, 400]
[0, 7,000]
C
% Super-permissive
% cells per field of view
p=0.00238
p=0.0279
8 hpi
24 hpi
Victoria
B.1.1.7
D
SARS-CoV-2 genome coverage per strain
Counts normalised to total library counts and averaged across replicates (x10⁶)
B.1.1.7
Victoria
Hours post infection
2hpi
8hpi
24hpi
E
B.1.1.7 and Victoria samples
Percentage of reads mapping to SARS-CoV-2
2hpi
8hpi
24hpi
F
B.1.1.7 and Victoria samples
Percentage negative strand reads (of all SARS-CoV-2 reads)
2hpi
8hpi
24hpi
G
B.1.1.7 and Victoria samples
sgRNA/gRNA ratio
Ratio
p=0.016
p=5.5e-06
ns
p=0.055
2hpi
8hpi
24hpi

Figure S6

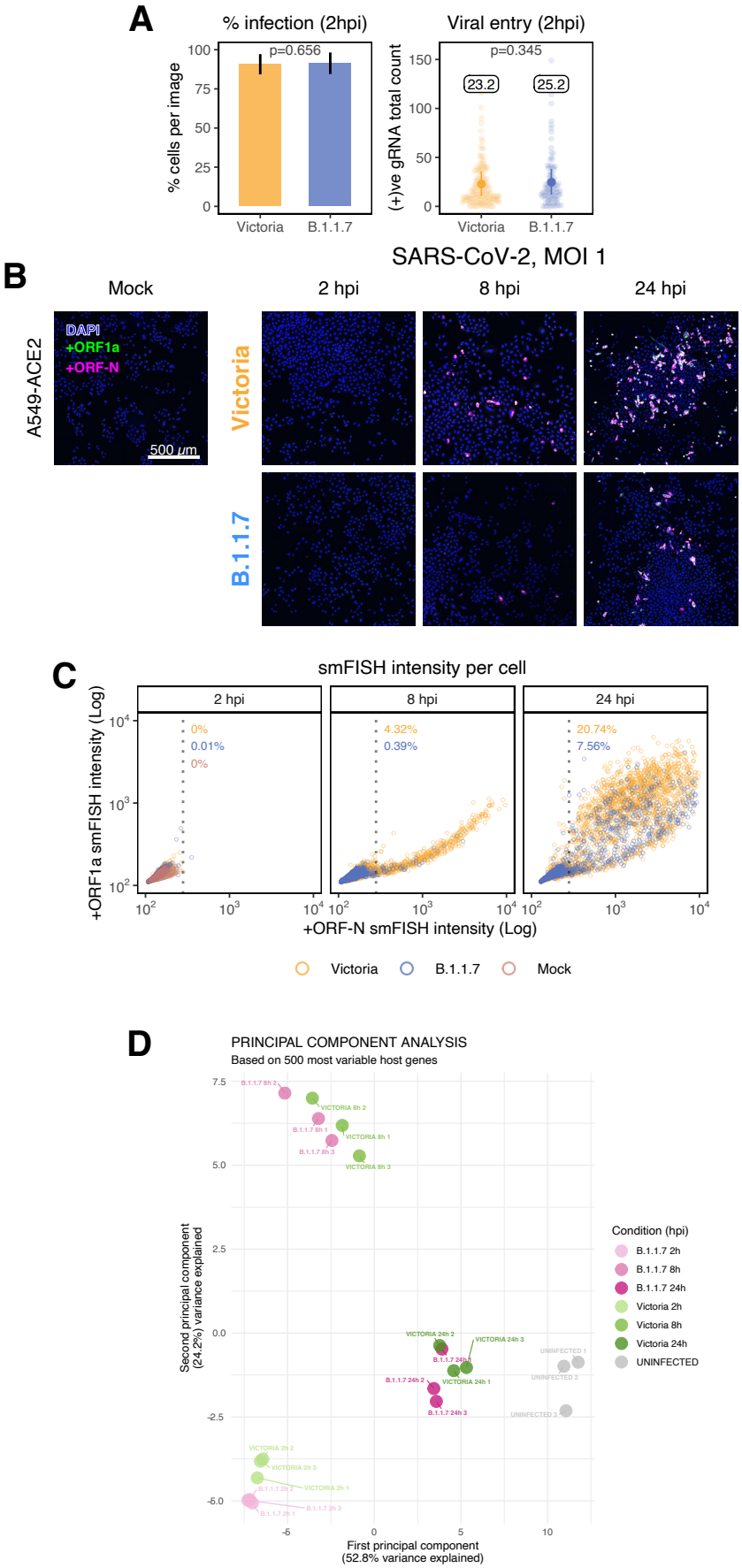
A
% infection (2hpi)
% cells per image
p=0.656
Victoria
B.1.1.7
Viral entry (2hpi)
(+)ve gRNA total count
p=0.345
23.2
25.2
B
SARS-CoV-2, MOI 1
Mock
2 hpi
8 hpi
24 hpi
A549-ACE2
DAPI
+ORF1a
+ORF-N
500 µm
Victoria
B.1.1.7
C
smFISH intensity per cell
2 hpi
8 hpi
24 hpi
+ORF1a smFISH intensity (Log)
+ORF-N smFISH intensity (Log)
0%
0.01%
0%
4.32%
0.39%
20.74%
7.56%
Victoria
B.1.1.7
Mock
D
PRINCIPAL COMPONENT ANALYSIS
Based on 500 most variable host genes
Second principal component (24.2%) variance explained
First principal component (52.8% variance explained)
Condition (hpi)
B.1.1.7 2h
B.1.1.7 8h
B.1.1.7 24h
Victoria 2h
Victoria 8h
Victoria 24h
UNINFECTED